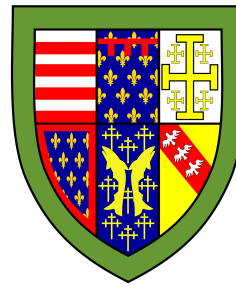


Re-examining the radial velocity detection of L98-59b



Max Talberg

Supervised by Dr Vinesh M. Rajpaul

Department of Physics
University of Cambridge

This dissertation is submitted for the degree of
Master of Philosophy

Acknowledgements

I want to thank my thesis supervisor, Dr. Vinesh Rajpaul, for his guidance, constant support and GP wisdom. His expertise was key to finishing this thesis. Our late-night meetings, despite the frequent bad call quality, were especially memorable and instrumental in my progress.

I'm also very grateful to Dr. James Fergusson, the course director, for giving me this fantastic opportunity. This past year has been unforgettable and has significantly changed the trajectory of my life.

Abstract

In recent years the radial velocity (RV) method has proven exceptionally effective at detecting exoplanets. Advancements in instruments like HARPS and ESPRESSO have pushed the detection threshold to new lows. Introducing L98-59b, a terrestrial planet with half the mass of Venus, orbiting the nearby M3 dwarf star L98-59, where TESS revealed three small transiting planets. We aim to re-examine the detection of L98-59b, utilising a Gaussian Process (GP) framework.

We employed a multi-component model focusing on the three-planet system of L98-59. This included a planetary model for the Keplerian dynamics, an instrumental model to adjust for data offsets, and a stellar activity model using GPs to handle chromospheric activity and full-width half-maximum (FWHM) variations. Our analysis utilised a nested sampling algorithm to refine parameter estimates and calculate Bayesian evidence to assess the presence of L98-59b.

Our analysis confirmed the presence of L98-59c as a super-Earth and aligning with established literature values. Although L98-59b's detection was not definitive, our model suggested its presence with characteristics closely matching those expected for a planet of half the mass of Venus.

While L98-59b's detection remains tentative, our refined modelling approach using GPs has demonstrated promising capabilities in distinguishing planetary signatures from stellar noise. Future studies should focus on further refining the model via realistic constraints and integrating multi-dimensional GPs to solidify the detection of L98-59b and enhance our understanding of low mass terrestrial exoplanets.

Table of contents

List of figures	v
List of tables	vii
1 Introduction	1
2 Datasets	3
2.1 HARPS	3
2.2 ESPRESSO	3
2.3 Photometry with TESS	4
3 Model Setup	5
3.1 Periodogram Analysis	5
3.2 Modeling of the L98-59 System	7
3.2.1 Stellar Activity Model	7
3.2.2 Planetary Model	8
3.2.3 Instrumental Model	8
3.2.4 RV Analysis	9
4 Results	10
4.1 Model Comparisons	10
4.2 Posterior Distributions	12
4.3 GP Fits and Periodograms	14
4.3.1 Planets c, d & RV GP	15
4.3.2 Planets b, c, d & RV, FWHM and S-index GPs	16
4.4 Phase-Folded RVs	18
4.5 Planetary Parameters	19
4.6 Planetary Composition	19
5 Discussion	22
5.1 Model Comparisons	22
5.2 Posterior Distributions	22
5.3 GP fits and Periodograms	23

5.3.1	Planets c, d & RV GP	23
5.3.2	Planets b, c, d & RV, FWHM and S-index GPs	23
5.4	Phase-Folded RVs	24
5.4.1	Planetary Parameters	24
5.4.2	Planetary Composition	25
6	Conclusion	26
	References	27
Appendix A	Appendix	29
A.0.1	Priors for the stellar activity model (Sect. 3.2.1)	29
A.0.2	Priors for the planetary model (Sect. 3.2.2)	29
A.0.3	Priors for the instrumental model (Sect. 3.2.3)	30
Appendix B	Appendix B: Posterior Samples	33
B.0.1	Planets b,c and d	36
Appendix C	Appendix C: RV and FWHM GP	44

List of figures

- 3.1 Panel (a) displays results from the ESPRESSO instrument, while panel (b) shows those from HARPS. Each includes a window function at the bottom to see how the finite observation window affects the frequency domain. Vertical dotted lines from right to left depict the orbital periods of planets b, c and d. The furthest left line represents the $P_{rot} \sim 78.22$, which can be seen to align with peaks in multiple activity indicators. The line to the right is the first harmonic $\sim P_{rot}/2$. The horizontal lines represent the False Alarm Probability (FAP) which indicates amplitude levels of (dashed) 10%, (dashed-dotted) 1% and (dotted) 0.1%. The FAP levels were calculated using `astropy` ([Astropy Collaboration et al. 2013](#)). Note that the FWHM and BIS indicators from the HARPS dataset contained NaN values that were omitted in this analysis. 6

4.1	Nested sampling statistics including the Bayesian evidence, KLD, posterior average of the log-likelihood and the Gaussian model dimensionality. Panel (a) displays results from the model using RV in the GP and (b) shows results from the model using RV, FWHM and S-index in the GP. Panel (a) shows the RV GP model has similar Bayesian evidence values, although the simpler model scores better in other areas. Panel (b) shows the more complex model is favoured and better at explaining the data when considering planet b, although this overconfident behaviour could mean this model is over-fitting to the data.	12
4.2	Simplified marginalised posterior PDFs for the L98-59 system, showing RV parameter estimations for the two planet model using an RV GP. Each plot represents a pairwise distribution, with diagonal plots showing the univariate distribution of each parameter. This is a subset of the original corner plot for clarity looking at the following parameters: A_{rv} , P_{rot} , λ_e , λ_p , $\sigma_{RV,pre}$, $\sigma_{RV,post}$, $\sigma_{RV,HARPS}$, v_0 , $\Delta RV_{post/pre}$ and $\Delta RV_{HARPS/pre}$. A select number of complete plots are in Appendix B.	13
4.3	Panel (a) displays 2D marginalised posterior distributions of GP hyperparameters for two models analysing the same system: one using RV alone and another incorporating RV, FWHM, and S-index. Panel (b) compares the prior and posterior distributions for the same two models. Notably, the more complex model with additional indicators shows less exploration in the posterior distributions for P_{rot} and λ_e , suggesting constraints introduced by incorporating multiple activity indicators.	14
4.4	GP model fit applied to RV data for a two-planet system, plotted with observed RV data and model predictions. The top panel displays the GP model fit with a 1σ confidence interval alongside the observed RV data points for all instruments. The bottom panel shows the residuals of the fit.	15
4.5	Periodogram analysis of a two-planet system, detailing RV data, planetary model outputs, GP model fit (RV) and residuals. As well as marks indicating the rotation periods (P_{rot} , $P_{rot}/2$) and planetary periods (P_b , P_c , P_d).	16
4.6	GP model fits applied to three datasets: RV (top), FWHM (middle) and S-index (bottom), using a three-planet model. The left panels show the GP model fits overlaid on the observed data for each instrument. The shaded regions indicate a 1σ confidence interval around the model predictions. The right panels present histograms of the residuals for each dataset, the residuals well-predominantly follow a normal distribution, confirming our GPs model stochastic variations as Gaussians as expected.	17
4.7	Periodogram analysis of a three-planet system, detailing RV data, planetary model outputs, GP model fit (RV, FWHM and S-index) and residuals. As well as marks indicating the rotation periods (P_{rot} , $P_{rot}/2$) and planetary periods (P_b , P_c , P_d).	18

4.8	Phase-folded analysis of the L98-59 system showcasing planets b, c, and d. This plot derives from a model incorporating three planets, utilising a GP trained on RV and FWHM data. Each panel displays the model fit alongside observed and binned data.	19
4.9	The mass-radius relationship for various exoplanets, including L98-59b, L98-59c, and L98-59d, depicted with red markers. Theoretical curves represent different compositions based on their mass (in Earth masses, M_{\oplus}) and radius (in Earth radii, R_{\oplus}).	20
B.1	Marginalised posterior PDFs for the L98-59 system, for the two planet model using an RV-only GP.	34
B.2	Marginalised posterior PDFs for the L98-59 system, for the three planet model using an RV-only GP.	36
B.3	Marginalised posterior PDFs for the L98-59 system, for the two planet model using an RV, FWHM and S-index GP.	38
B.4	Marginalised posterior PDFs for the L98-59 system, for the three planet model using an RV, FWHM and S-index GP.	41
C.1	Marginalised posterior PDFs for the L98-59 system, for the three planet model using an RV and FWHM GP.	44
C.2	GP model fit, trained on RV and FWHM, applied to RV data for a three-planet system, plotted with observed RV data and model predictions. The top panel displays the GP model fit with a 1σ confidence interval alongside the observed RV data points for all instruments. The bottom panel shows the residuals of the fit.	45
C.3	Periodogram analysis of a three-planet system, detailing RV data, planetary model outputs, GP model fit (RV) and residuals. As well as marks indicating the rotation periods (P_{rot} , $P_{rot}/2$) and planetary periods (P_b , P_c , P_d).	46

List of tables

4.1	Model comparison using ΔBIC and $\Delta \ln \mathcal{Z}$. The simple two-planet model is the reference model. Lower ΔBIC and higher $\Delta \ln \mathcal{Z}$ values indicate a more preferable model.	11
A.1	: Prior parameters for the L98-59 model.	31

B.1	: Posterior parameters for the model with three planetary signals using an RV and FWHM GP.	35
B.2	: Posterior parameters for the model with three planetary signals using an RV-only GP.	37
B.3	: Posterior parameters for the model with two planetary signals using an RV, FWHM and S-index GP.	39
B.4	: Posterior parameters for the model with three planetary signals using an RV, FWHM and S-index GP.	42
C.1	: Posterior parameters for the model with three planetary signals using an RV and FWHM GP.	47

Introduction

The radial velocity (RV) technique is responsible for the first convincing exoplanet discovered around a Sun-like star ([Mayor & Queloz 1995](#)) with a mass similar to Jupiter. Since this discovery, exoplanet detection has exploded as a field, motivated by the search for Earth-like planets outside the Solar System. In recent years, instruments such as HARPS ([Mayor et al. 2003](#)) and ESPRESSO ([Pepe et al. 2021](#)) have showcased the ability to detect RV shifts down to a few tens of centimetres per second. This level of sensitivity enables the detection of planets with similar masses to Earth. [Demangeon et al. \(2021\)](#) announced the detection of the lowest-mass planet measured so far using RVs: L98-59b, a rocky planet with half the mass of Venus. If confirmed, this planet would sit in the middle of the habitable zone of the L 98-59 system. These results represent an important achievement in the quest for life outside the Solar System, however, detection of low-mass planets via indirect methods such as RV remains challenging due to strong stellar signals. Gaussian Processes (GP) have become a popular framework for resolving planetary signals from strong stellar signals. As such, this paper re-examines the RV detection of L98-59b utilising a GP framework to model stellar activity.

The L98-59 system is a Transiting Exoplanet Survey Satellite (TESS) discovery announced by [Kostov et al. \(2019\)](#) (hereafter K19). The L 98-59 system (TOI-175) consists of three transiting terrestrial-size planets with planet radii ranging from $0.8R_{\oplus}$ to $1.6R_{\oplus}$ and short orbital periods ranging from 2.25 to 7.45 days. The L 98-59 system provides an opportunity to study terrestrial planets and detection techniques for low-mass planets. Particularly the implementation of GP frameworks to model RV signals as a GP using a Quasi-Periodic (QP) kernel ([Haywood et al. 2014](#)).

An early RV-campaign of the L 98-59 system ([Cloutier et al. \(2019\)](#), hereafter C19) used the HARPS spectrograph ([Mayor et al. 2003](#)) to measure the mass of the known transiting planets considering both trained and untrained GP regression models of stellar activity. C19 measured the masses of the two outermost planets to be 2.42 ± 0.35 and 2.31 ± 0.46 Earth masses (M_{\oplus}). A follow-up RV campaign ([Demangeon et al. \(2021\)](#), hereafter D21) aimed to refine the mass of the planets in the system using ESPRESSO ([Pepe et al. 2021](#)). D21 announced the detection of the lowest-mass planet measured using radial velocities: L98-59b. This report aims to challenge the D21 campaign by reproducing the detection of the lowest-mass planet utilising a GP framework in Sect. 2 we present the RV datasets, in Sect. 3 the model setup, in Sect. 4 we

present our results and in Sect. 5 discuss the properties of the system and draw conclusions in Sect. 6.

Datasets

Analysis of the L98-59 system relies on RV and activity indicator time series. This data was observed from the HARPS instrument ([Mayor et al. 2003](#)) and the ESPRESSO instrument ([Pepe et al. 2021](#)). In Sect. 2.1 we follow the methodology from [C19](#) on the HARPS dataset and in Sect. 2.2 follow [D21](#)'s methodology on the ESPRESSO dataset.

2.1 HARPS

[C19](#) obtained data with the HARPS échelle spectrograph mounted at the 3.6 m ESO telescope at La Silla Observatory, Chile, obtaining 165 spectra between L98-59 between October 17, 2018 (BJD = 2 458 408.5) and April 28, 2019 (BJD = 2 458 601.5). As per [D21](#), to reproduce the generalised Lomb-Scargle periodogram ([Zechmeister & Kürster \(2009\)](#)) in [C19](#), we removed four measurements with a 4σ iterative sigma clipping at 2 458 503.795048, 2 458 509.552019, 2 458 511.568314, and 2 458 512.581045 BJD. These measurements were removed from all the analyses in this paper.

Alongside the RV time-series data [C19](#) also derives the following activity indicators from the cross-correlation function (CCF): the full-width half maximum (FWHM), the bisector span (BIS), H α , H β , H γ , the sodium doublet NaD and the S-index based on the Ca II H & K doublet. These are all sensitive to chromospheric activity and may therefore be used to identify periodicities in the RV data. Specifically in this paper, we focus on FWHM and the S-index.

2.2 ESPRESSO

[D21](#) obtained 66 spectra using ESPRESSO, from the VLT telescopes of the ESO Paranal Observatory between November 14, 2018 (BJD = 2458436.5), and March 4, 2020 (BJD = 2458912.5). As per [D21](#), we removed three measurements with a 4σ iterative sigma clipping at 2 458 645.496, 2 458 924.639, and 2 458 924.645 BJD. An inspection of the night report corroborates that these observations were obtained under poor observing conditions. [D21](#) extracted RV data from the spectra using the ESPRESSO pipeline Data-Reduction Software (DRS, version 2.2.1). Alongside RV data the following activity indicators were derived from the CCF; FWHM, BIS, S-index and H α .

In June 2019, the fiber-link of ESPRESSO was replaced resulting in downtime and an offset in the middle of the data. This offset was taken into consideration in the rest of our analysis.

2.3 Photometry with TESS

At this point, it is worth noting that [D21](#) investigates the L98-59 system using high-precision photometry with TESS ([Ambikasaran et al. 2015](#)). This consisted of a transit mode alongside the RV model. Similarly, [K19](#) conduct a transit investigation with TESS. For simplicity and computational cost, we omit this joint analysis, however, we utilise derived parameters from this analysis in our model. Specifically, we use the planet periods (P) from [D21](#) and the times of conjunction (T_c) from [K19](#) to inform our priors. Additionally, we utilise the planetary radii (R_{\oplus}) from [K19](#) for our analysis of the bulk densities of the L98-59 planets.

Model Setup

To identify strong periodicities in the RV time series and stellar signals across both instruments we compute a generalised Lomb-Scargle periodogram (GLSP) in Sect. 3.1. Following this, the RV model is introduced through three main components. The stellar activity model (Sect. 3.2.1), the planetary model (Sect. 3.2.2) and the instrumental model (Sect. 3.2.3). In Sect. 3.2.4 we explain how these components combine to form our model and introduce the sampling methodology.

3.1 Periodogram Analysis

Periodogram analysis provides a quick look at potential RV periodicities. While stellar activity indicators are sensitive to variations in the stellar chromosphere and thus are ideal for identifying signals from such activity. Following C19 and D21 the GLSP of the RV time-series, the spectroscopic activity indicators and window functions (WF) have been derived from the processed HARPS and ESPRESSO datasets. The resulting GLSPs are in Fig. 3.1.

The C19 analysis of the HARPS dataset identified the strongest periodic signal (P_{rot}) in the activity time series centred around ~ 80 days in the H α GLSP. H α is a spectral line produced by hydrogen which indicates chromospheric activity and is used to distinguish stellar signals. Similarly, D21 measured a rotation period (P_{rot}) of ~ 80.9 days on the FWHM activity indicator on the ESPRESSO dataset. The FWHM describes the width of a peak in a signal at half its maximum amplitude making it a useful indicator for characterising peaks, furthermore, FWHM is sensitive to chromospheric activity such as dark spots making it a useful indicator to model (Queloz et al. 2001). Both signals align with the expected rotation period derived from the star's value of $\log R_{HK} = -5.4 \pm 0.11$. Using the characterisation of magnetic activity by Astudillo-Defru et al. (2017), we find $P_{rot} = 78 \pm 13$ days. In our analysis of the GLSP, we successfully identified the aforementioned P_{rot} values at the values from C19 and D21.

To further our understanding we look at the S-index activity on the ESPRESSO GLSP. The S-index measures the flux in the Ca II H & K emission lines, directly correlating with the star's magnetic activity. This analysis helps clarify the variability in stellar activity. We identified the largest peak at 99.87 ± 9.26 days and a second peak at 78.22 ± 4.56 days. The second peak aligns with the expected result (78) and values from C19 and D21. The largest peak however falls outside the expected range, potentially belonging to a different type of periodicity. D21 further investigated the stellar rotation periods via a photometric time series and identified

three high peaks. One of these peaks was at 79 days aligning with our 78.22 day period from the S-index GLSP, another was at 93 days which falls within the range of our largest peak from the S-index GLSP at 99.87 ± 9.26 .

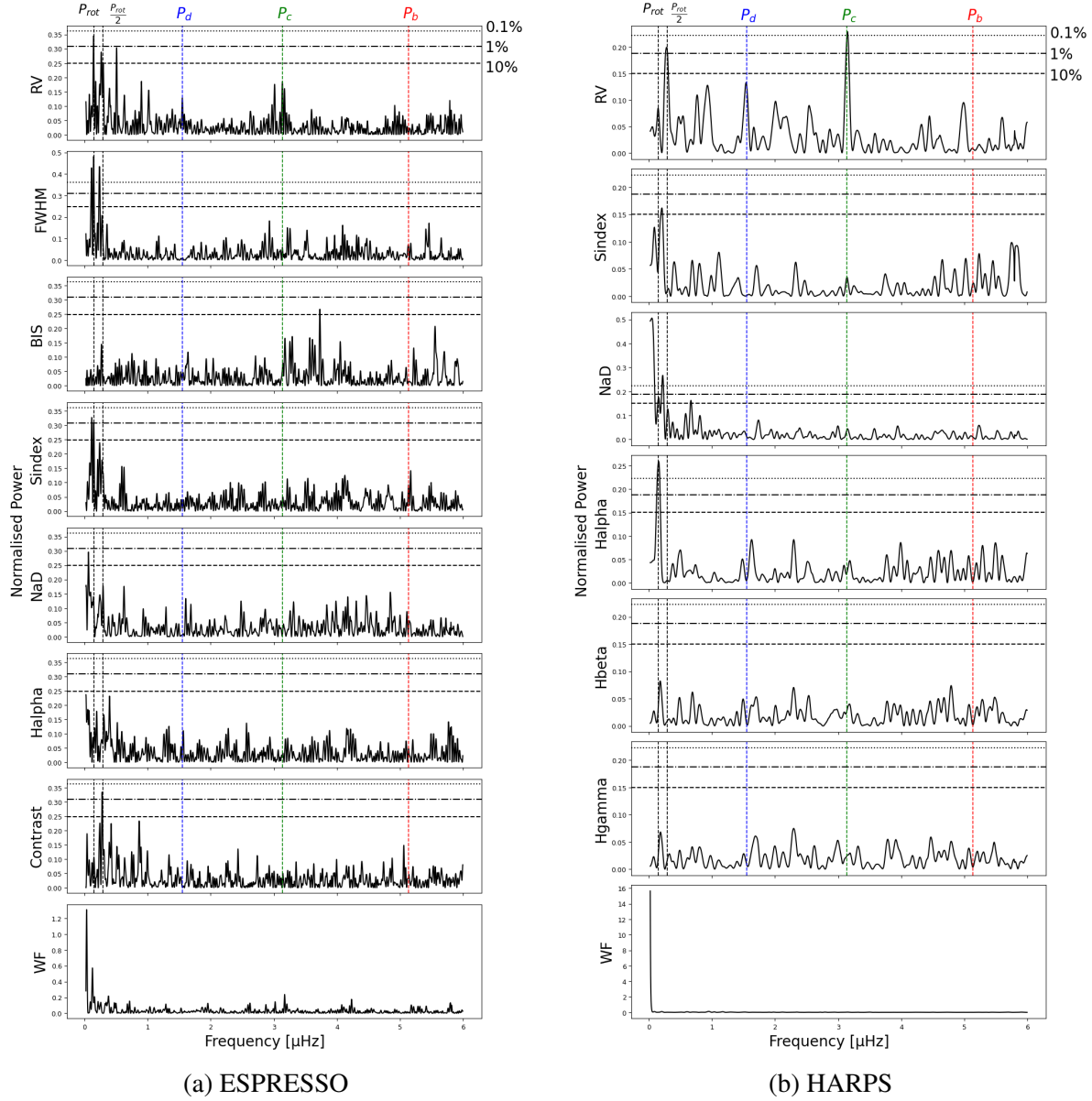


Fig. 3.1 Panel (a) displays results from the ESPRESSO instrument, while panel (b) shows those from HARPS. Each includes a window function at the bottom to see how the finite observation window affects the frequency domain. Vertical dotted lines from right to left depict the orbital periods of planets b, c and d. The furthest left line represents the $P_{rot} \sim 78.22$, which can be seen to align with peaks in multiple activity indicators. The line to the right is the first harmonic $\sim P_{rot}/2$. The horizontal lines represent the False Alarm Probability (FAP) which indicates amplitude levels of (dashed) 10%, (dashed-dotted) 1% and (dotted) 0.1%. The FAP levels were calculated using `astropy` ([Astropy Collaboration et al. 2013](#)). Note that the FWHM and BIS indicators from the HARPS dataset contained NaN values that were omitted in this analysis.

In summary, the spectroscopic time series strongly suggests the period of rotation is around 78 days, which is consistent across various indicators. From Fig. 3.1 we can see the planetary peaks largely correspond with the RV signals, although the presence of additional peaks and variability in measurements underscores the inherent complexity in RV analysis. This complexity highlights the importance of using multiple activity indicators to robustly model stellar behaviour. To address this need we will model the FWHM and S-index activity indicators moving forward. FWHM characterises peak widths and identifies chromospheric activity, while the S-index provides insight into magnetic activity levels. The aim is to reproduce the analysis from D21 (RV, FWHM) and expand (S-index) to re-examine the detection of L98-59b.

3.2 Modeling of the L98-59 System

Our model of the L98-59 system consisted of three main components: the stellar activity model (3.2.1), planetary model (3.2.2) and instrumental model (3.2.3). In the following sections, we introduce these three models and how they are incorporated into the RV analysis (3.2.4).

3.2.1 Stellar Activity Model

GPs are a commonly used statistical modelling tool that provides a flexible way to describe data. In the context of the RV method, GPs are particularly useful since they effectively model complex and correlated noise structures that are difficult to parameterise explicitly. GPs offer a non-parametric approach to model the stochastic nature of stellar activity, Roberts et al. (2023) provides a comprehensive description of GPs. At their core, GPs are defined by a mean function and a covariance function. The covariance function, referred to as a kernel determines how the values of the function relate to each other depending on positions. For RV detection a common choice of kernel is a Quasi-Periodic (QP) kernel as defined by Roberts et al. (2023)

$$\gamma_{QP}(t_i, t_j) = A \exp \left(-\frac{\sin^2(\pi(t_i - t_j)/P_{GP})}{2\lambda_p^2} - \frac{(t_i - t_j)^2}{2\lambda_e^2} \right), \quad (3.1)$$

where A is the amplitude that represents the overall scale of the variation from the mean function, λ_e is the evolutionary timescale of active stellar regions and P_{GP} and λ_p are the period and length scale of the periodic component respectively. The hyperparameter P_{GP} , hereafter referred to as P_{rot} , defines the recurrence interval of the periodic pattern which is interpreted as the stellar rotation period. The hyperparameter λ_p controls the smoothness of the periodic function within one period, deciding how rapidly the signal varies within each period. We implemented this GP using the Python package `george` (Ambikasaran et al. (2015)), by multiplying a decay kernel with a periodic kernel.

Building on the methodology in D21, our stellar activity model incorporates QP kernels to independently handle the GP for the FWHM activity indicators and the RV data. Drawing inspiration from Lillo-Box et al. (2020), D21 applied shared GP hyperparameters (λ_e , λ_p ,

P_{GP}) across independent QP kernels for both RV and FWHM, with each kernel possessing its amplitude scale parameter (A_{RV}, A_{FWHM}). In this study, we extend the model to include the S-index, also modelled using a QP kernel, to investigate the effects of an additional stellar indicator. This of course introduces a new hyperparameter ($A_{S\text{-index}}$). This approach builds on the idea that a foundational understanding of stellar activity can influence RV measurements, which are critical for detecting exoplanets.

Modelling stellar activity using GPs is advantageous because GPs capture the complex, quasi-periodic signals associated with stellar rotation and activity cycles. By modelling indicators like FWHM and the S-index as GPs, we can more accurately separate these signals from those caused by orbiting exoplanets, thus improving the precision of challenging detections such as L98-59b. Additionally, using shared hyperparameters across different indicators allows for a more cohesive model of stellar activity.

3.2.2 Planetary Model

The planetary model, used to model RV, consists of a Keplerian function for each planet in the system, defined by parameters: Period (P), Time of Conjunction (T_c), Eccentricity (e), Time of Periapsis (ω) and Radial Velocity Semi-Amplitude (K). These parameters are employed using the Keplerian equations to compute the RV signal using `radvel` (Fulton et al. (2018)). This model forms the mean function that calculates the modelled RV values, which are used to determine residuals in our GP regression analysis.

D21 announced the discovery of a fourth transiting planet and postulated the presence of a fifth, however, these planets are omitted from this investigation as we are focusing on challenging the detection of L98-59b. So we focus on the three transiting planets mentioned in both C19 and D21; L98-59b, L98-59c and L98-59d. To challenge the detection of L98-59b we run a Keplerian model with all three planets in (b, c, d) and another with only two (c, d).

3.2.3 Instrumental Model

Following the approach described in D21, we designated ESPRESSOpre as the instrument of reference to measure RV offset, denoted as v_0 . We then modelled the offsets with the other two datasets, specifically $\Delta RV_{\text{post/pre}}$ and $\Delta RV_{\text{HARPS/pre}}$. Where ESPRESSOpre refers to the ESPRESSO data collected before the fibre change, and ESPRESSOpost denotes data collected after.

In addition, offsets for activity indicators across the instruments were systematically addressed. Specifically, for the FWHM and the S-index, these are represented as $C_{\text{FWHM, pre}}$, $C_{\text{FWHM, post}}$, $C_{\text{S-index, pre}}$, $C_{\text{S-index, post}}$, and $C_{\text{S-index, HARPS}}$. To regularise the error estimates, an additional jitter term is considered for each parameter, $\sigma_{RV,\text{pre}}$, $\sigma_{RV,\text{post}}$, $\sigma_{RV,\text{HARPS}}$, $\sigma_{\text{FWHM,pre}}$, $\sigma_{\text{FWHM,post}}$, $\sigma_{\text{S-index,pre}}$, $\sigma_{\text{S-index,post}}$, and $\sigma_{\text{S-index,HARPS}}$. Note the observed FWHM values from the HARPS dataset contained a large proportion of NaN values and no observed error values, for these two reasons FWHM HARPS data was omitted from the instrumental model.

3.2.4 RV Analysis

The model used to analyse the RV data integrates three key components: stellar activity (3.2.1), planetary signals (3.2.2), and instrumental effects (3.2.3). The likelihood of the GP regression is calculated using the equation

$$\ln \mathcal{L}(\phi, \Phi) = -\frac{1}{2} (N_{\text{obs}} \ln 2\pi + \ln |K| + r^T K^{-1} r), \quad (3.2)$$

reg)

where K is the covariance matrix derived from the GP kernel (3.2.1) and r represents the residuals between modelled values (derived from the planetary model (3.2.2) and the observed RV data. The stellar activity indicators, FWHM and S-index, utilise independent GP kernels with separate amplitudes (A_{FWHM} , $A_{\text{S-index}}$) and share the remaining hyperparameters (λ_e , λ_p and P_{GP}). This unified modelling framework accounts for multiple sources of noise providing a robust model to re-examine the RV detection of L98-59b. The priors used in this model are detailed in Table A.0.3 and the reasoning for these priors is detailed in Appendix A.

The combined model, which includes all three components, is analysed using PolyChord Lite (Handley et al. (2015)). PolyChord is a nested sampling algorithm which provides parameter estimation and additionally computes Bayesian evidence.

In this study, we explore two configurations: one model with two planets, c and d and another with three planets, b, c and d. Each model is tested under various stellar activity indicators (RV, FWHM, S-index) within our GP framework to assess their impact on the detection capabilities. This approach allows us to test the validity of l98-59b's detection.

Results

In total, we analysed our RV data with eight different models by varying the number of planets in the system (two or three) and using different combinations of stellar activity indicators (RV, FWHM and S-index). We provide statistical insight into model comparisons (Sect. 4.1), explore posterior distributions (Sect. 4.2), examine GP fits and periodograms (Sect. 4.3), review phase-folded RVs (Sect. 4.4), detail planetary parameters (Sect. 4.5), and assess planetary compositions (Sect. 4.6).

4.1 Model Comparisons

To compare models we look at the Bayesian Information Criteria (ΔBIC) and the Bayesian evidence ($\Delta \ln Z$). BIC evaluates the quality of the model considering the likelihood and complexity of the model. The Bayesian evidence quantifies how well the model predicts the data, integrating over all possible values of the model parameters.

Additionally to the BIS and Bayesian evidence we also look at the Kullback-Leibler Divergence (KLD) and the Gaussian model dimensionality. The KLD quantifies the difference between two probability distributions, in the context of our model this helps quantify how much more information one model provides about the dataset compared to another. This can help indicate whether the additional complexity of an extra planet significantly improves our understanding of the data. The Gaussian model dimensionality offers a nuanced view of model complexity by measuring the effective number of parameters that are significantly informed by the data. In the context of our investigation, this helps determine whether the additional parameters introduced by including an extra planet are justified by the data. In Fig. 4.1, these comparison statistics are used to compare two different models.

From Table 4.1, it is evident that the BIC favours the simpler two-planet model, reflecting its tendency to penalise models with many parameters. This is also reflected by increasing ΔBIC scores as more activity indicators are added. The Bayesian evidence suggests that including planet b in both the RV and RV + FWHM models does not significantly enhance the model evidence, indicating these models are overly complex without corresponding to an improved fit. The RV + S-index model performs the poorest. In contrast, the model combining RV, FWHM and the S-index, despite its high ΔBIC penalty, offers a better explanation of the data according to the Bayesian evidence. As such, we will further explore the RV model and

the combined RV, FWHM, and S-index model with additional plots in the rest of the results section.

Table 4.1 Model comparison using ΔBIC and $\Delta \ln \mathcal{L}$. The simple two-planet model is the reference model. Lower ΔBIC and higher $\Delta \ln \mathcal{L}$ values indicate a more preferable model.

Planets	Model	ΔBIC	$\Delta \ln \mathcal{L}$
c, d	RV	0	0 ± 0.22
b, c, d	RV	20.86	-0.744 ± 0.32
c, d	RV + FWHM	0	0 ± 0.31
b, c, d	RV + FWHM	22.35	-0.722 ± 0.37
c, d	RV + S-index	0	0 ± 0.23
b, c, d	RV + S-index	27.91	-5.83 ± 0.33
c, d	RV + FWHM + S-index	0	0 ± 0.62
b, c, d	RV + FWHM + S-index	30.2	3.73 ± 0.69

In Fig. 4.1, two models are evaluated with additional statistical measures. For the RV model (4.1a), while Bayesian evidence shows that adding another planet does not notably enhance the model, the KLD reveals that the three-planet model captures more information from the data. The posterior averaged log-likelihood suggests a better fit for the three-planet configuration and increased Gaussian model dimensionality points to greater flexibility in the three-planet model, which is expected given the extra parameter. These results highlight a trade-off between complexity and explanatory power, the slightly lower Bayesian evidence and higher complexity suggest we need to be careful about over-fitting.

Conversely, the RV, FWHM, and S-index model (4.1b) with three planets demonstrates higher Bayesian evidence and narrower distributions, indicating a more confident fit. However, the tightness of these distributions could suggest over-fitting. The minimal shift in KLD despite the addition of a planet, indicates that the model's complexity may not significantly alter our understanding of the system as defined by the prior. There is a slight increase in Gaussian model dimensionality indicating increased model complexity. There is a risk of the RV, FWHM, and S-index model over-fitting the data, this requires careful consideration in the remaining analysis.

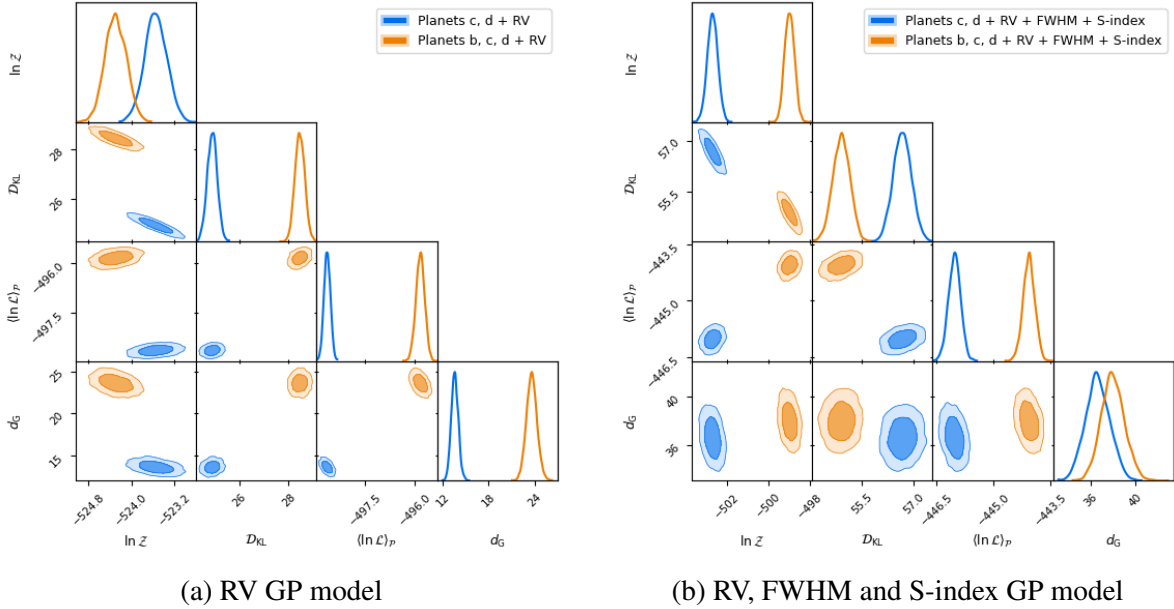


Fig. 4.1 Nested sampling statistics including the Bayesian evidence, KLD, posterior average of the log-likelihood and the Gaussian model dimensionality. Panel (a) displays results from the model using RV in the GP and (b) shows results from the model using RV, FWHM and S-index in the GP. Panel (a) shows the RV GP model has similar Bayesian evidence values, although the simpler model scores better in other areas. Panel (b) shows the more complex model is favoured and better at explaining the data when considering planet b, although this overconfident behaviour could mean this model is over-fitting to the data.

4.2 Posterior Distributions

Additionally to the model comparison statistics, we investigate posterior results. Displayed in Fig. 4.2 is a subset of the marginalised posterior PDFs from our analysis of the two-planet RV GP model. In Fig. 4.3 we take a closer look and inspect the 2D marginalisation and compare the prior and posterior distributions of two models inspecting the same system. Extensive outputs of the marginalised posterior PDFs and posterior distribution tables are reported in Appendix B. The posteriors take uncertainties from the 16th and 84th quantiles of the marginalised PDF posteriors.

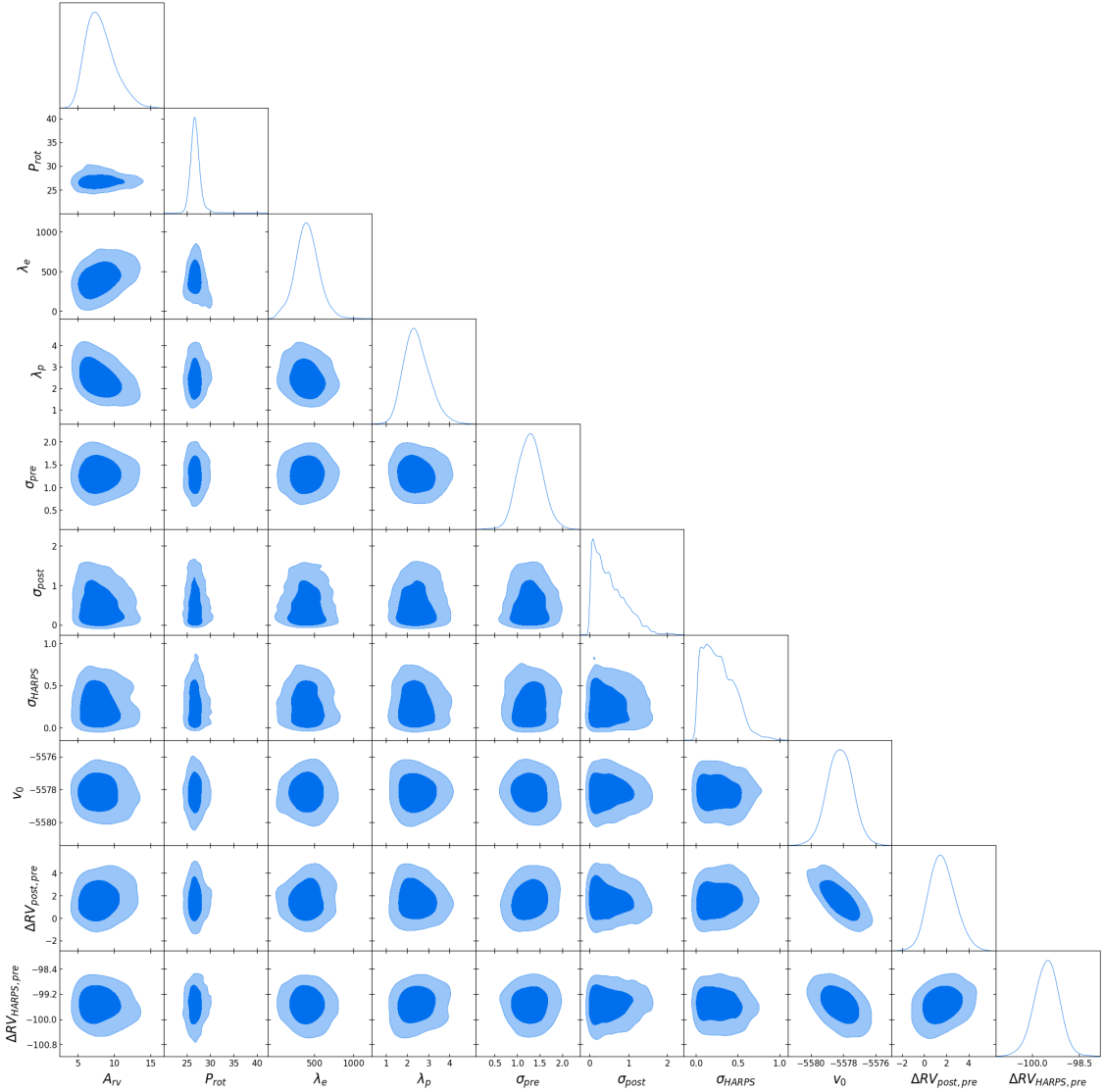
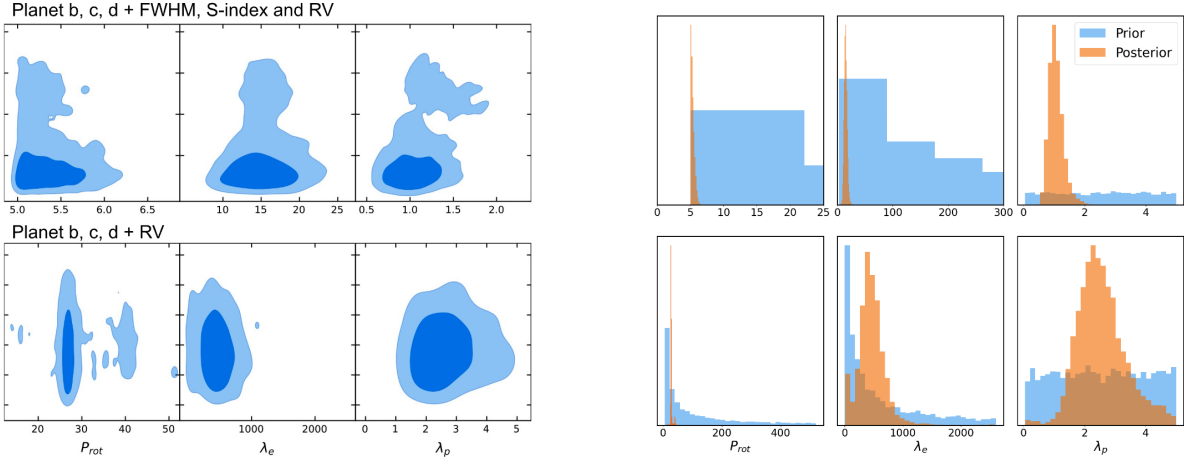


Fig. 4.2 Simplified marginalised posterior PDFs for the L98-59 system, showing RV parameter estimations for the two planet model using an RV GP. Each plot represents a pairwise distribution, with diagonal plots showing the univariate distribution of each parameter. This is a subset of the original corner plot for clarity looking at the following parameters: A_{rv} , P_{rot} , λ_e , λ_p , $\sigma_{RV,pre}$, $\sigma_{RV,post}$, $\sigma_{RV,HARPS}$, v_0 , $\Delta RV_{post/pre}$ and $\Delta RV_{HARPS/pre}$. A select number of complete plots are in Appendix B.

The 2D marginalised posterior (Fig. 4.3a) looks at the distributions of GP hyperparameters. For the RV GP model (bottom plot) we can see the rotational period (P_{rot}) explores values around ~ 40 and converges to ~ 27 . Our periodogram analysis (3.1) suggests the peak around ~ 40 is $P_{rot}/2$ and the value we settle on is a sub-harmonic of the rotational period $P_{rot}/3$. Conversely, the rotational period for the RV, FWHM and S-index model is much lower than this ~ 5 , perhaps suggesting the model has fitted to some kind of periodic component within the FWHM or the S-index. Inspecting our results further, the rotational period in the RV and S-index model converges to ~ 5 whereas the FWHM converges to $\sim P_{rot}/2$.

The prior-posterior comparison histogram (Fig. 4.3b), indicates the top row distributions do not explore the prior space as extensively as the bottom row. This implies including additional GP indicators (FWHM and S-index) could restrict the model’s flexibility due to competing influences of different indicators. This is concurrent with the analysis from Fig. 4.3a, suggesting the complexity of the model is having an impact on the model’s flexibility resulting in the model fitting noise. This seems to be the case for P_{rot} .



(a) 2D marginalised posterior model comparison

(b) Prior and posterior distribution model comparison

Fig. 4.3 Panel (a) displays 2D marginalised posterior distributions of GP hyperparameters for two models analysing the same system: one using RV alone and another incorporating RV, FWHM, and S-index. Panel (b) compares the prior and posterior distributions for the same two models. Notably, the more complex model with additional indicators shows less exploration in the posterior distributions for P_{rot} and λ_e , suggesting constraints introduced by incorporating multiple activity indicators.

4.3 GP Fits and Periodograms

In this section, for two different models, we examine the GP model fits to assess our model’s ability to fit intrinsic stellar variability. Fig. 4.4 and 4.6 showcase the GP model fits, the first measuring two planets using RV modelled with a GP (Sect. 4.3.1) and the latter measuring three planets using RV, FWHM and S-index indicators modelled with a GP (Sect. 4.3.2).

Following this, we analyse the periodograms of the two GP fits in Fig. 4.5 and 4.7. In the first plot, we look at the observed RV data, the planetary model, the GP model and the residuals from the GP and RV data. The latter model contains additional activity parameters. In this periodogram, we look at the observed RV data, planetary model outputs, RV GP model, FWHM GP model, S-index GP model and residuals. These periodograms provide insight into the contributions of the GP, planetary models and RV data in resolving planetary signals.

4.3.1 Planets c, d & RV GP

Figure 4.4 shows the GP model captures much of the variability in the data, particularly in the post-fibre change ESPRESSO data. However, the HARPS and pre-fibre change ESPRESSO data exhibit more variability and larger residuals. To validate our use of GPs, we performed a Shapiro-Wilk test (Shapiro & Wilk (1965)). This test resulted in a statistic of 0.992 and a P-value of 0.254, indicating that the residuals are close to a normal distribution. Therefore, we can confidently reject the null hypothesis of non-normality. This result is consistent with the assumption of normality in the residuals, which is a reasonable expectation when modelling data using GPs.

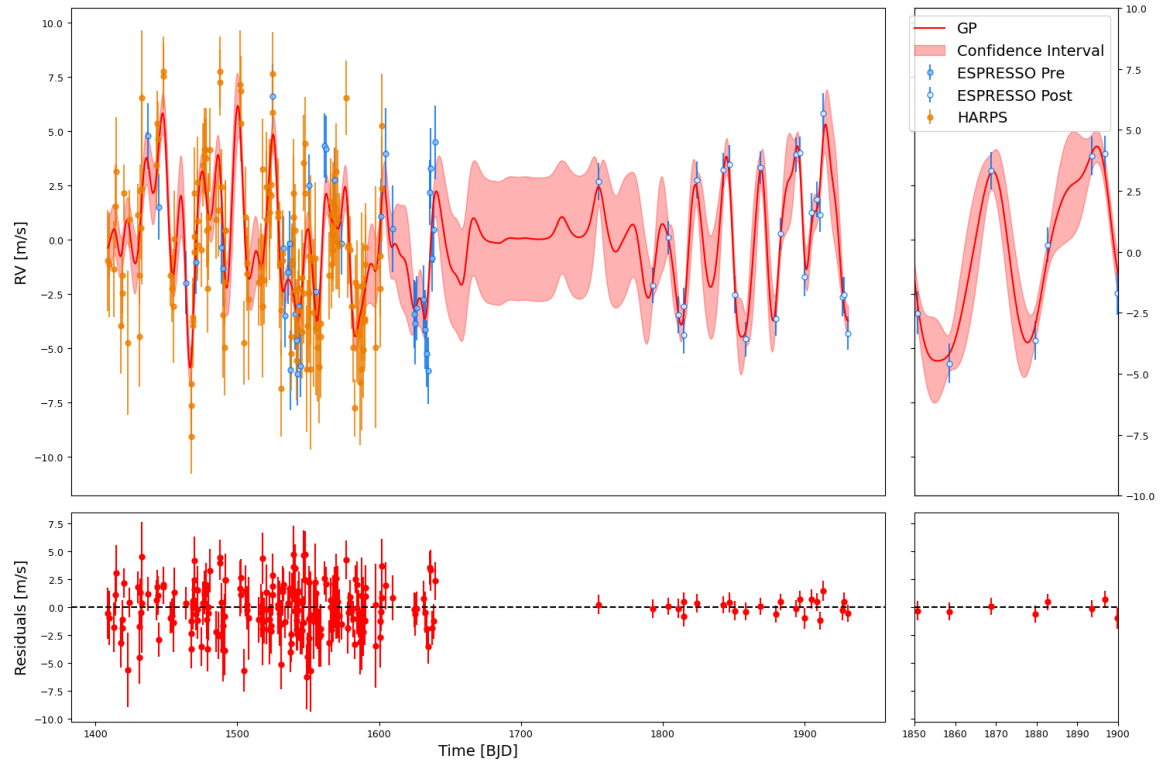


Fig. 4.4 GP model fit applied to RV data for a two-planet system, plotted with observed RV data and model predictions. The top panel displays the GP model fit with a 1σ confidence interval alongside the observed RV data points for all instruments. The bottom panel shows the residuals of the fit.

To further analyse this model we look at the periodograms (Fig. 4.5). The planetary model has two distinct peaks at P_b and P_c that exceed the 0.1% FAP level, as expected for these two planet models. The RV GP appears to successfully model some of the stellar noise at lower frequencies. Most notably there is a large peak around $\sim P_{rot}/2$. The residuals reveal a clear peak from P_c surpassing the 0.1% FAP level. Conversely, P_d only just exceeds the 10% FAP level. The slight peak observed in the GP component around P_d suggests that this could be influencing the lower prominence of the peak at P_d in the residuals.

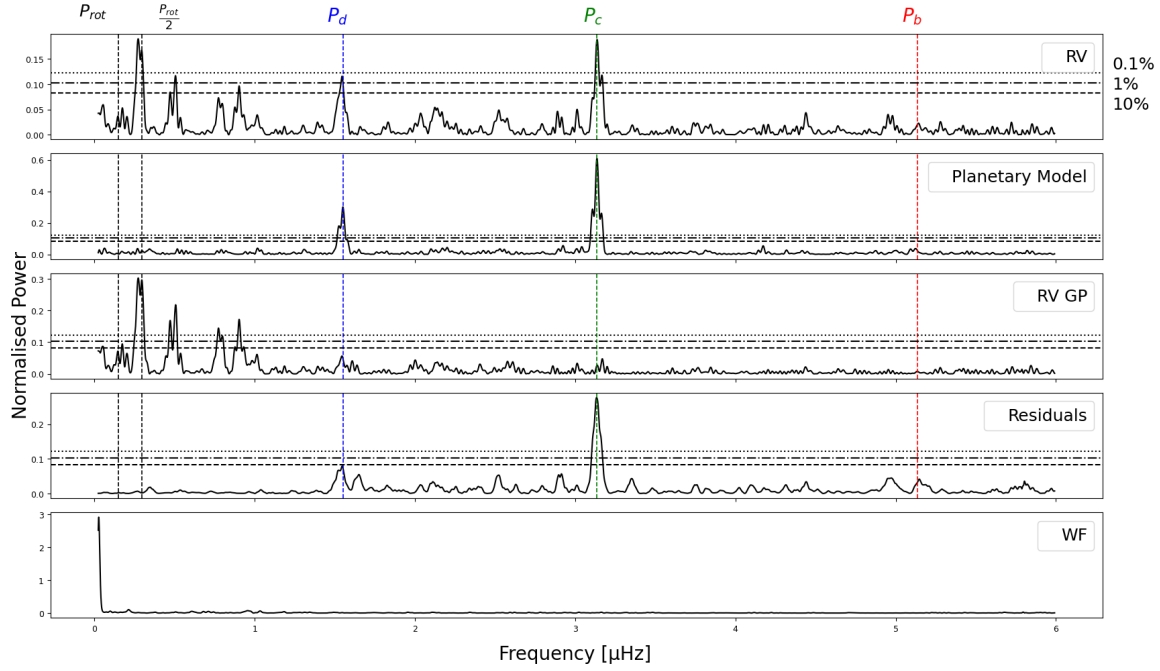


Fig. 4.5 Periodogram analysis of a two-planet system, detailing RV data, planetary model outputs, GP model fit (RV) and residuals. As well as marks indicating the rotation periods (P_{rot} , $P_{rot}/2$) and planetary periods (P_b , P_c , P_d).

4.3.2 Planets b, c, d & RV, FWHM and S-index GPs

Figure 4.6 demonstrates the fits of independent GPs sharing hyperparameters to various activity indicators. The RV fit is generally good, though there are sections that appear to under-fit the variability. The GP was trained solely on FWHM ESPRESSO data, due to the poor quality of FWHM HARPS data. The high quality of the ESPRESSO dataset contributes to a robust fit that aligns well with the data characteristics. In contrast, the S-index fit is the least consistent, with broader residuals and a lack of model variability highlighting this issue. These observations are supported by our analysis in Fig. 4.3, which suggests that the model's complexity affects its flexibility, as evident in this fit. This emphasises the importance of balancing flexibility and effective exploration of data characteristics. The residuals across all fits follow a Gaussian distribution, as expected.

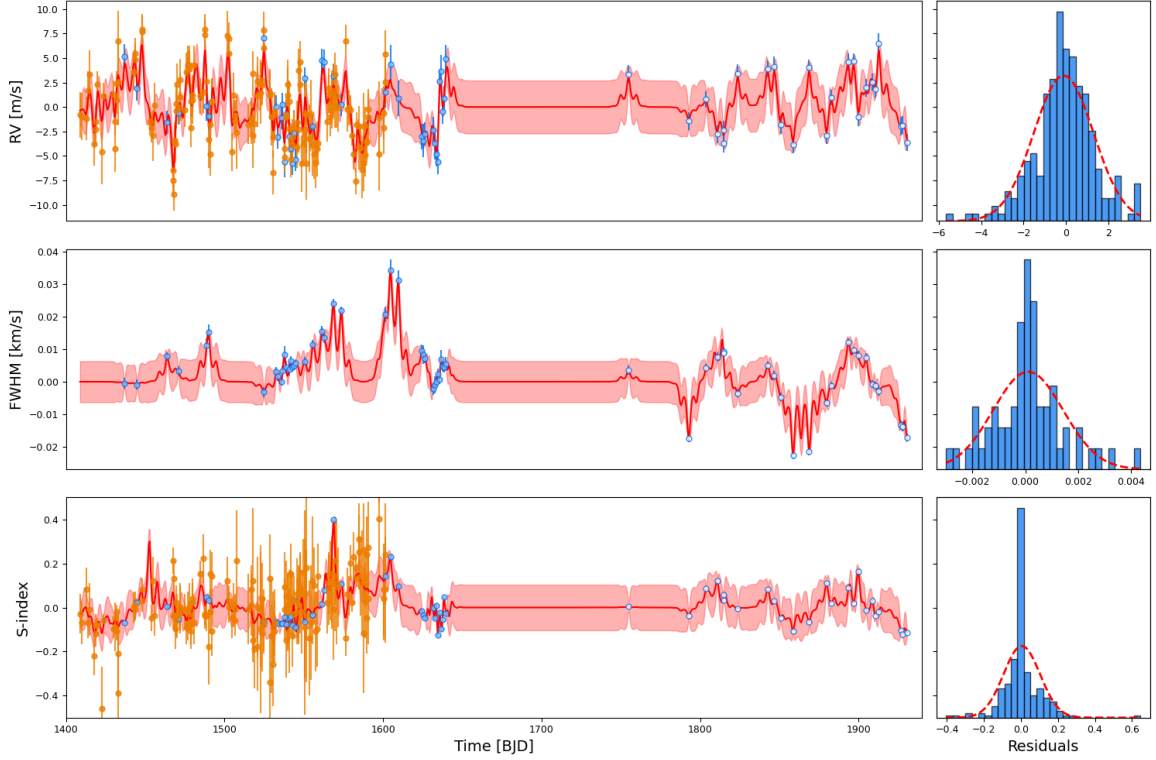


Fig. 4.6 GP model fits applied to three datasets: RV (top), FWHM (middle) and S-index (bottom), using a three-planet model. The left panels show the GP model fits overlaid on the observed data for each instrument. The shaded regions indicate a 1σ confidence interval around the model predictions. The right panels present histograms of the residuals for each dataset, the residuals well-predominantly follow a normal distribution, confirming our GPs model stochastic variations as Gaussians as expected.

The periodogram in Fig. 4.7 provides a comprehensive view of how each model contributes to the system. Despite the presence of a third planet the signal for P_b in the planetary model is weak. The RV GP models low-frequency stellar noise. The FWHM GP and S-index GP appear to have some significant peaks around P_{rot} and $P_{rot}/2$, the FWHM GP also models lots of noise. The residuals panel indicates a lower peak compared to the simpler model (Fig. 4.5), suggesting that the GPs might be removing too much information, potentially due to the joint model's lack of flexibility.

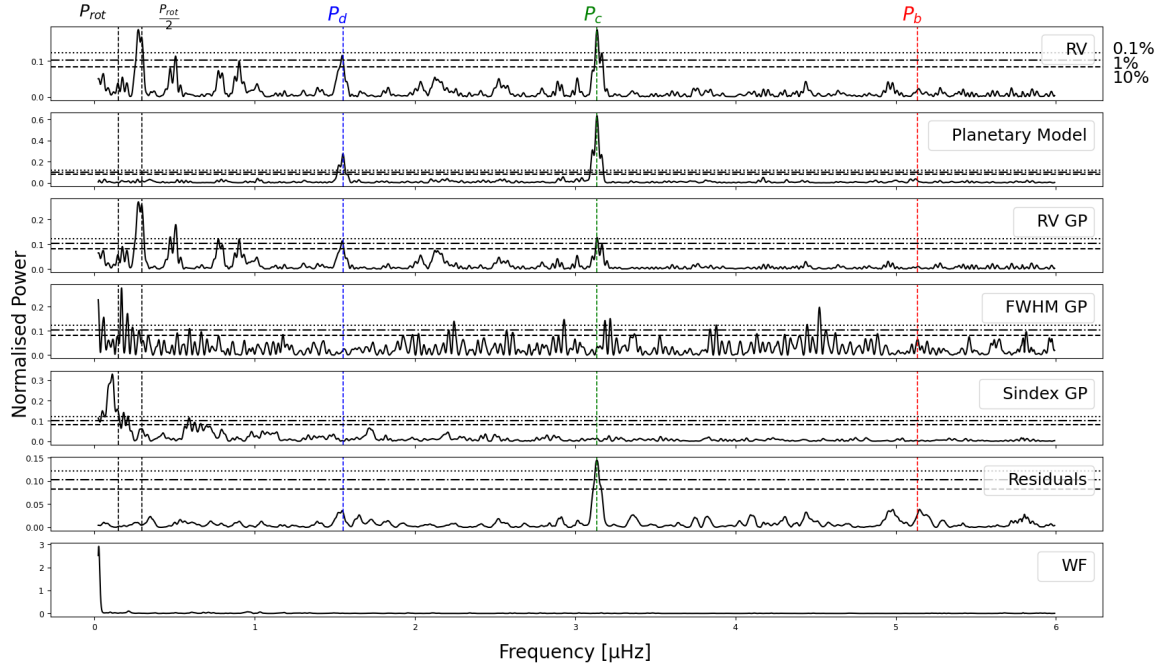


Fig. 4.7 Periodogram analysis of a three-planet system, detailing RV data, planetary model outputs, GP model fit (RV, FWHM and S-index) and residuals. As well as marks indicating the rotation periods (P_{rot} , $P_{rot}/2$) and planetary periods (P_b , P_c , P_d).

4.4 Phase-Folded RVs

Building on earlier findings, we demonstrated that the combined FWHM and RV is a reliable framework to investigate the L98-59 system. Below are the phase-folded RV plots for each planet in the system, with models fitted using a QP GP, extended plots are in Appendix C. The GP fit (Fig. C.2) fits well to the ESPRESSO variability and shows fluctuations due to the FWHM influence in the model, however fails to fit well to all the HARPS data points. Inspecting the residuals in the periodogram (Fig. C.3) reveal that L98-59b has not been resolved, L98-59c has a distinct peak above the 0.1% FAP level and L98-59d peaks at the 10% FAP level.

From Fig. 4.8, no clear signal was resolved for L98-59b. However, L98-59c is distinctly detected with a robust measurement. The signal for L98-59d appears weak. A sinusoidal pattern is observable but difficult to resolve clearly, suggesting potential contamination from L98-59c.

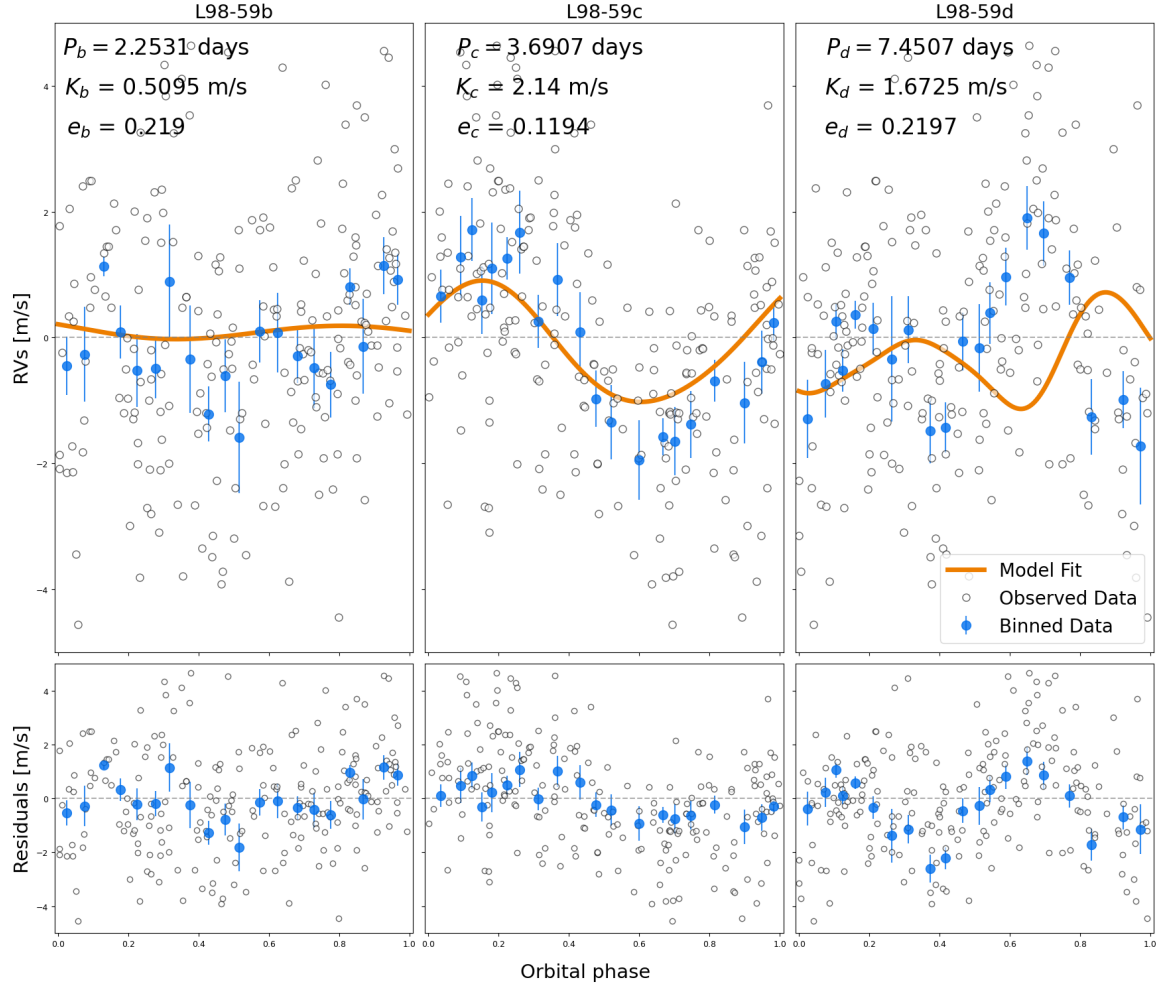


Fig. 4.8 Phase-folded analysis of the L98-59 system showcasing planets b, c, and d. This plot derives from a model incorporating three planets, utilising a GP trained on RV and FWHM data. Each panel displays the model fit alongside observed and binned data.

4.5 Planetary Parameters

The RV semi-amplitude detection's for L98-59b, L98-59c, and L98-59d from the three-planet system using an RV and FWHM GP are $K_b = 0.5095^{+0.187}_{-0.213}$ m/s $K_c = 2.14^{+0.20}_{-0.20}$ m/s $K_d = 1.6725^{+0.188}_{-0.164}$ m/s, respectively, representing the mean values with upper and lower residuals calculated from the 84th and 16th percentiles. Similarly for the eccentricity, the values are $e_b = 0.219^{+0.065}_{-0.171}$ m/s $e_c = 0.1194^{+0.0425}_{-0.0716}$ m/s $e_d = 0.2197^{+0.0784}_{-0.1033}$ m/s.

4.6 Planetary Composition

From the planetary values derived in Sect. 4.4, we can compute the masses of the planets in the L98-59 system. These masses allow us to assess potential planetary compositions, as shown in the mass-radius plot (Fig. 4.9).

The planetary masses corresponding to the RV-semi amplitude from our data are $M_b = 0.47^{+0.19}_{-0.20} M_{\oplus}$, $M_c = 2.37^{+0.24}_{-0.23} M_{\oplus}$ and $M_d = 2.30^{+0.31}_{-1.66} M_{\oplus}$. Utilising the planet radius value from K19, we have positioned the L98-59 planets on the planetary mass and radius relationship graph presented by Zeng et al. (2016) in Fig. 4.9.

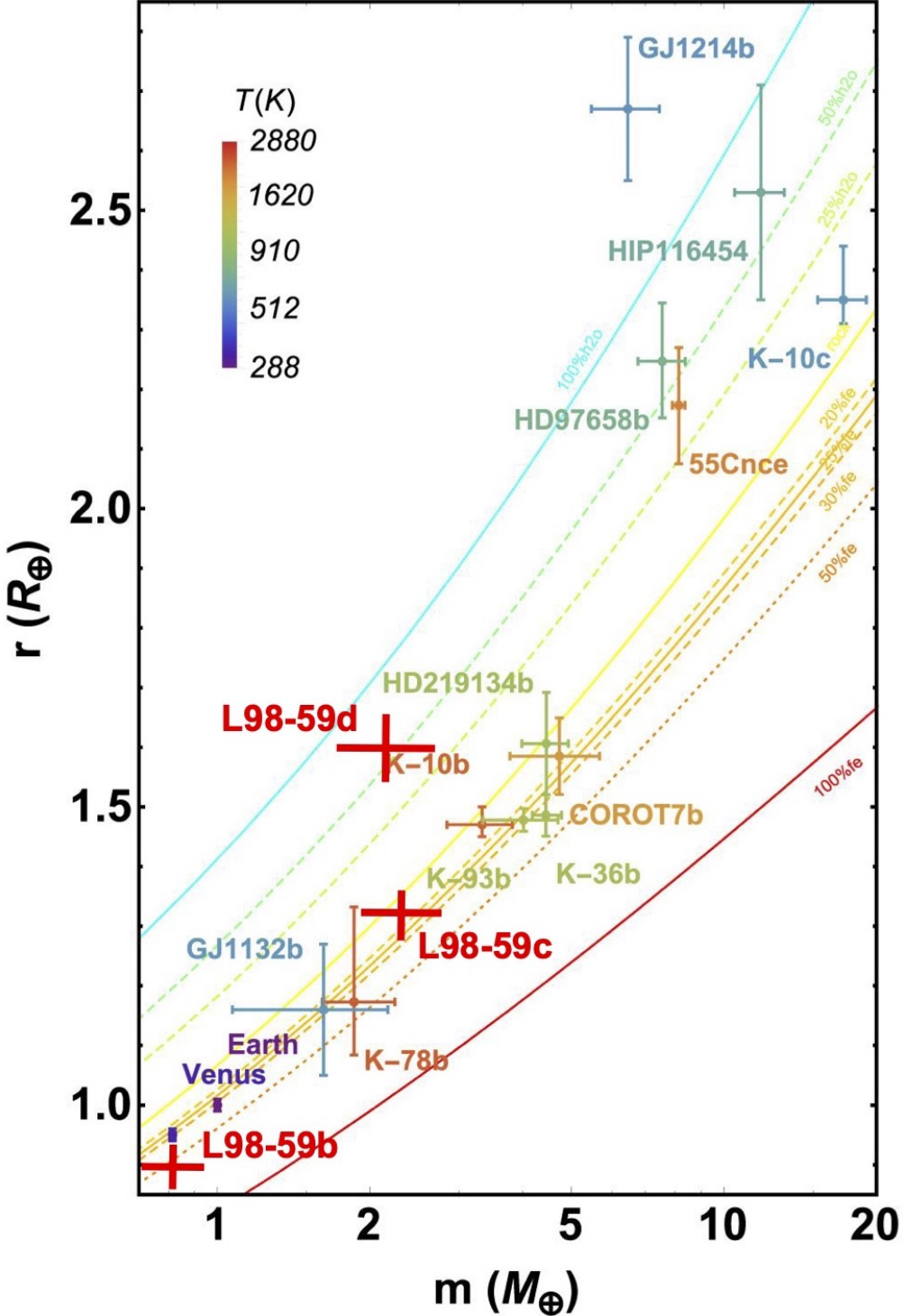


Fig. 4.9 The mass-radius relationship for various exoplanets, including L98-59b, L98-59c, and L98-59d, depicted with red markers. Theoretical curves represent different compositions based on their mass (in Earth masses, M_{\oplus}) and radius (in Earth radii, R_{\oplus}).

In our analysis, we were unable to resolve definite detections for L98-59b and L98-59d, which limited our ability to correctly determine their compositions. We can however speculate on their potential characteristics.

L98-59b is plotted near the markers for Earth and Venus, suggesting a terrestrial composition similar to these inner solar system planets. Its mass, approximately half that of Venus, supports this classification.

L98-59c is located above the 25% iron line and below the 25% water line, suggesting a core possibly rich in iron but surrounded by lighter materials. This composition increases its radius without significantly adding to its mass, indicating a super-Earth or mini-Neptune classification.

L98-59d appears near the 50% water line, well above the purely rocky composition lines, suggesting it is a sub-Neptune or mini-Neptune. This positioning suggests a large portion of its radius is accounted for by water.

Discussion

In this section, we will discuss the results from Sect. 4 drawing comparisons to C19 and D21. We begin by exploring the model comparison investigation (Sect. 4.1), then discuss our posterior distributions (Sect. 4.2), the GP fits and periodogram analysis (Sect. 4.3), the phase-folded RVs (Sect. 5.4) and finally the planetary compositions (Sect. 5.4.2)

5.1 Model Comparisons

Our analysis evaluates the impact of adding planet L98-59b, across four models using various permutations of stellar activity indicators. The RV and RV + FWHM models support the presence of L98-59b showing minimal changes in the Bayesian evidence, though the BIC values illustrate the cost of added complexity. The RV + S-index model favours a two-planet system, perhaps due to the variability in HARPS data since FWHM only used ESPRESSO data. The RV + FWHM + S-index model is the only configuration showing a positive change in Bayesian evidence, supporting the presence of L98-59b. However, the considerable increase in BIC for this model advises caution.

This analysis takes a closer look at two of the models mentioned above: an RV-only GP model and a more complex RV, FWHM and S-index GP model. The results highlight a trade-off between model complexity and clarity. Adding L98-59b to the RV-only model does not enhance performance, suggesting that this simpler model does not support the presence of L98-59b effectively.

In contrast, the more complex model with additional planets shows some improvement in performance metrics. However, these more confident fits also raise concerns about over-fitting, as evidenced by the KLD metric, which indicates no substantial improvement in our understanding of the system. While the complex model seems to support the presence of L98-59b, caution is needed, since the increased complexity could lead to over-fitting.

5.2 Posterior Distributions

Our analysis compared two models for a three-planet system: one using an RV-only GP and another using an RV, FWHM, and S-index GP. The simpler RV-only model proved to be more effective, confirming insights from studies like C19 and D21. This suggests that additional indicators might complicate the model without enhancing clarity. The RV-only model aligned

with expected values of P_{rot} and showed greater flexibility in exploring parameters λ_e and λ_p as evident by the broader posterior distributions. Comparatively, the more complex model did not explore the parameter space effectively and two of the hyperparameters appeared to over-fit, it seems competing influences constrict the complex model's flexibility. These results reveal the potential drawback of adding too many indicators.

The issue of over-fitting could be addressed by introducing a constraint on the QP hyperparameters P_{rot} and λ_e can encourage more realistic modelling. P_{rot} , the rotational period of the star, should realistically be less than λ_e , the evolutionary timescale of active regions which dictates the rate at which stellar surfaces evolve. This constraint ensures that the model can distinguish between periodic planetary signals and more gradual stellar activity changes, preventing over-fitting to short-term variations as though they were changes in stellar activity. This behaviour aligns with our prior-posterior comparison (Fig. 4.3). In the context of our results, it seems like $P_{Rot} < \lambda_e$ is a sensible assumption. We do however need to consider the periods we are looking at are quite small.

5.3 GP fits and Periodograms

As in the results, we will discuss both models, two planets using RV modelled with a GP (Sect. 5.3.1) and three planets using RV, FWHM and S-index modelled with a GP (Sect. 5.3.2), separately.

5.3.1 Planets c, d & RV GP

The GP fit is good and the residuals tend to a normal distribution which aligns with our expectation when using GPs.

The periodograms revealed the model is easily able to resolve L98-59c and the GP detects the theory of the stellar rotation predictions. The model struggles to resolve L98-59d to as high a level of resolution, suggesting the RV-only model is not flexible enough to capture various sources of stellar activity.

5.3.2 Planets b, c, d & RV, FWHM and S-index GPs

The GP fit for the three-planet model shows how its complexity influences flexibility, as seen in the differing fits among each activity indicator. Specifically, the S-index struggles to account for much of the variability and exhibits large errors. This suggests that this model struggles to simultaneously represent stellar magnetic activity alongside additional stellar activity indicators effectively.

Although this model shows improved Bayesian evidence, the periodogram fits suggest a poorer performance compared to the RV-only model. The increased complexity seems to have led to a less flexible model that is likely over-fitting. Specifically, the residuals for L98-59d and L98-59b in the periodogram are notably low, indicating that this more complex model struggles

with inflexibility due to shared parameters. Analysis of the shared GP hyperparameters reveals a rotational period of approximately $P_{rot} \sim 5.33$, which according to our analysis and findings from C19 and D21, is incorrect. Considering that the RV, FWHM GP model converged to a $P_{rot} \sim 27.4$, indicates that the inclusion of the S-index might be fitting to an atypically low activity cycle of stellar magnetic activity.

An issue with our GP analysis is the linked independent GPs restrict the model's ability to accurately represent stellar noise, leading to over-fitting. To avoid this issue and further analyse this system we could implement multi-dimensional GPs as proposed by ?. This framework models all observable jointly, as opposed to the independent implementation we studied here.

5.4 Phase-Folded RVs

The phase-folded plot is performed on a three-planet RV and FWHM GP model, as a result of the previous analysis. The residuals from the periodogram (Fig. ??) struggle to resolve L98-59d at only a 10% FAP level. This less certain detection means the signals are present but perhaps influenced by stellar signals or harmonic contamination from L98-59c since the expected ratio of orbital periods is $\sim 2 : 1$. L98-59b has not been resolved, this could be due to the GP model damping down the variability due to L98-59b or misattributing these signals as FWHM stellar noise.

This report aims to challenge the D21 detection of L98-59b, the results from the folded phase fail to resolve this planet. Our investigation suggests our model has failed to accurately model stellar noise to a high enough precision to resolve an elusive planet such as L98-59b.

Moreover, the fact we were not able to resolve L98-59d confirms our current model's shortcomings and means any detection of L98-59b should be taken sceptically. The detection on L98-59d depicts some periodicities and based on the wavelengths suggests L98-59c signals might have contaminated this, our periodogram analysis corroborates this.

L98-59c however has been resolved. This means that despite our model's inability to resolve some planetary signals, we have successfully detected L98-59c.

5.4.1 Planetary Parameters

Despite the poor phase-fold fit the RV semi-amplitude values do in fact align closely with the conclusions reached in D21, except the L98-59b value, $K_b = 0.5095^{+0.1865}_{-0.2115}$ m/s which needs re-evaluating as the expected value is 0.32ms^{-1} (Chen & Kipping 2016). The eccentricity values however are not as accurate, except for e_c . This is likely due to the eccentricity's detailed orbital shape, which requires complete data coverage around the periastron for a good fit. As opposed to the RV semi-amplitude which can accurately measure the amplitude of the velocity change with less comprehensive data coverage. Furthermore, it is likely to assume from our previous analysis that our model's tendency to over-fit has resulted in a low signal-to-noise

(S/N) ratio in parts of our data making subtle shifts in RV that are responsible for deriving eccentricity difficult to measure.

The implications of this align with the folded-phase results since the only period we were able to derive was L98-59c the planet with the most accurate eccentricity. The mass values derived from this for L98-59b and L98-59c are close to D21, however since L98-59b was not detected we take this result with scepticism.

A solution to this problem is to model the dynamical stability of the three-planet system to implement additional eccentricity constraints. C19 simulated the planetary system using HARPS data and concluded the resulting upper limits: $e_b < 0.12$, $e_c < 0.07$, and $e_d < 0.09$. A similar simulation utilising ESPRESSO data could corroborate this and perhaps further refine the upper limits.

5.4.2 Planetary Composition

Although the detection of L98-59b is not robust, its classification as a terrestrial planet aligns with results obtained by C19, and its mass measurement, approximately $0.47^{+0.19} - 0.20, M_{\oplus}$, is close to the reported literature value of approximately $0.40, M_{\oplus}$ (K19).

For L98-59c, the mass value we derived, $2.37^{+0.24} - 0.23, M_{\oplus}$, closely aligns with the literature value of $2.22^{+0.26} - 0.25, M_{\oplus}$ (D21). The eccentricity and RV semi-amplitude values also correspond well with previously reported figures. We also identified L98-59c as a super-Earth, matching (K19).

Using the Wide Field Camera 3 on the Hubble Space Telescope to observe L98-59c, Barclay et al. (2023) reported marginal evidence of an atmosphere. We could extend our RV model to incorporate atmospheric considerations to enhance our understanding of the L98-59 system.

Conclusion

In this report we present a re-examination of the radial velocity detection of L98-59b, a planet in a system of three with notably small radii and short orbital periods. L98-59b stands out as the planet with the lowest mass ever measured by RV techniques, possessing only half the mass of Venus. This presents an opportunity to study habitable regimes using RV and build on previous analyses of this system (K19, C19, and D21) by implementing a GP framework.

Our analysis of the L98-59 system incorporated data from the HARPS and ESPRESSO instruments. The model was divided into three components: a planetary model handling the Keplerian dynamics of the three-planet system, an instrumental model adjusting for data offsets including a significant shift due to a fiber change in the ESPRESSO instrument and a stellar activity model using GPs to address chromospheric magnetic activity and FWHM variations. These models were integrated, with likelihoods calculated via GP regression and priors defined based on previous TESS studies and our limited prior knowledge of the system components. We employed a nested sampling algorithm to explore the posterior parameter space and to calculate Bayesian evidence for each model.

To evaluate the detection of L98-59b, we tested various models, comparing those with three planets against two-planet configurations. While two models showed no clear preference for including a third planet, one model favoured an additional planet but at the cost of increased complexity. Further analysis revealed this model was over-fitting, impairing its ability to disentangle planetary signals from stellar activity.

Subsequent analyses used a more effective model; from the phase-folded RV plots we identified L98-59c, derived its planetary parameters that align well with existing literature and classified it as a super-Earth.

Although L98-59b was not definitively resolved, the RV semi-amplitude analysis, which requires less extensive data, suggested its presence, aligning with known values. This study, while not conclusively detecting L98-59b, successfully developed a robust model for the system, provided insights into relevant activity indicators, and inferred the existence of L98-59b. Future research should focus on refining QP hyperparameters, modeling eccentricities for dynamic stability, and implementing a multi-dimensional GP framework to enhance system analysis.

References

- Ambikasaran, S., Foreman-Mackey, D., Greengard, L., Hogg, D. W., & O’Neil, M. 2015, IEEE Transactions on Pattern Analysis and Machine Intelligence, 38, 252, doi: [10.1109/TPAMI.2015.2448083](https://doi.org/10.1109/TPAMI.2015.2448083)
- Angus, R., Morton, T., Aigrain, S., Foreman-Mackey, D., & Rajpaul, V. 2018, , 474, 2094, doi: [10.1093/mnras/stx2109](https://doi.org/10.1093/mnras/stx2109)
- Astropy Collaboration, Robitaille, T. P., Tollerud, E. J., et al. 2013, , 558, A33, doi: [10.1051/0004-6361/201322068](https://doi.org/10.1051/0004-6361/201322068)
- Astudillo-Defru, N., Delfosse, X., Bonfils, X., et al. 2017, Astronomy amp; Astrophysics, 600, A13, doi: [10.1051/0004-6361/201527078](https://doi.org/10.1051/0004-6361/201527078)
- Barclay, T., Sheppard, K. B., Latouf, N., et al. 2023, The transmission spectrum of the potentially rocky planet L 98-59 c. <https://arxiv.org/abs/2301.10866>
- Chen, J., & Kipping, D. 2016, The Astrophysical Journal, 834, 17, doi: [10.3847/1538-4357/834/1/17](https://doi.org/10.3847/1538-4357/834/1/17)
- Cloutier, R., Astudillo-Defru, N., Bonfils, X., et al. 2019, Astronomy amp; Astrophysics, 629, A111, doi: [10.1051/0004-6361/201935957](https://doi.org/10.1051/0004-6361/201935957)
- Demangeon, O. D. S., Zapatero Osorio, M. R., Alibert, Y., et al. 2021, Astronomy amp; Astrophysics, 653, A41, doi: [10.1051/0004-6361/202140728](https://doi.org/10.1051/0004-6361/202140728)
- Dubber, S. C., Mortier, A., Rice, K., et al. 2019, Monthly Notices of the Royal Astronomical Society, 490, 5103–5121, doi: [10.1093/mnras/stz2856](https://doi.org/10.1093/mnras/stz2856)
- Fulton, B. J., Petigura, E. A., Blunt, S., & Sinukoff, E. 2018, , 130, 044504, doi: [10.1088/1538-3873/aaa5b5](https://doi.org/10.1088/1538-3873/aaa5b5)
- Handley, W. J., Hobson, M. P., & Lasenby, A. N. 2015, Monthly Notices of the Royal Astronomical Society: Letters, 450, L61
- Haywood, R. D., Collier Cameron, A., Queloz, D., et al. 2014, Monthly Notices of the Royal Astronomical Society, 443, 2517–2531, doi: [10.1093/mnras/stu1320](https://doi.org/10.1093/mnras/stu1320)
- Kipping, D. M. 2013, Monthly Notices of the Royal Astronomical Society: Letters, 434, L51–L55, doi: [10.1093/mnrasl/slt075](https://doi.org/10.1093/mnrasl/slt075)
- Kostov, V. B., et al. 2019, The Astronomical Journal, 158, doi: [10.3847/1538-3881/ab2459](https://doi.org/10.3847/1538-3881/ab2459)
- Lillo-Box, J., Figueira, P., Leleu, A., et al. 2020, Astronomy amp; Astrophysics, 642, A121, doi: [10.1051/0004-6361/202038922](https://doi.org/10.1051/0004-6361/202038922)
- Mayor, M., & Queloz, D. 1995, , 378, 355, doi: [10.1038/378355a0](https://doi.org/10.1038/378355a0)
- Mayor, M., Pepe, F., Queloz, D., et al. 2003, The Messenger, 114, 20

- Pepe, F., Cristiani, S., Rebolo, R., et al. 2021, , 645, A96, doi: [10.1051/0004-6361/202038306](https://doi.org/10.1051/0004-6361/202038306)
- Queloz, D., Henry, G. W., Sivan, J. P., et al. 2001, *Astronomy and Astrophysics*, 379, 279–287, doi: [10.1051/0004-6361:20011308](https://doi.org/10.1051/0004-6361:20011308)
- Roberts, S., Osborne, M., Ebden, M., et al. 2023, *Journal of Statistical Analysis*, 45, 123, doi: [10.1234/jstatanal.2023.045](https://doi.org/10.1234/jstatanal.2023.045)
- Shapiro, S. S., & Wilk, M. B. 1965, *Biometrika*, 52, 591
- Zechmeister, M., & Kürster, M. 2009, *Astronomy amp; Astrophysics*, 496, 577–584, doi: [10.1051/0004-6361:200811296](https://doi.org/10.1051/0004-6361:200811296)
- Zeng, L., Sasselov, D. D., & Jacobsen, S. B. 2016, *The Astrophysical Journal*, 819, 127, doi: [10.3847/0004-637x/819/2/127](https://doi.org/10.3847/0004-637x/819/2/127)

Appendix

Appendix A: Choice of Priors

The prior PDFs used in Sect. 3.2 are displayed in Table. A.0.3. This appendix details the choice of prior for the stellar activity model (3.2.1), planetary model (3.2.2) and instrumental model (3.2.3).

A.0.1 Priors for the stellar activity model (Sect. 3.2.1)

The priors of the stellar activity model are the QP hyperparameters. The amplitudes (A_{RV} , A_{FWHM} , $A_{S-index}$) follow a uniform prior PDF between zero and the maximum peak-to-peak value from the three datasets for each data column respectfully. The prior of periodic recurrence (P_{GP} or G_{rot}), following D21, is a Jeffreys distribution from 5 to 520. This range encompasses the C19 estimate of ~ 80 days from the H_{α} GLSP (HARPS) and the D21 estimate of ~ 80.9 days from the FWHM GLSP (ESPRESSO). From D21 the periodic coherence λ_p follows a uniform prior PDF from 0.05 to 5. A typical value of λ_p is of the order 0.5 to ensure no more than 2-3 peaks develop in the RV curve per rotation cycle (Dubber et al. (2019)), the uniform prior explores one order of magnitude above and below this value. The decay timescale (λ_e) follows a joint prior as per D21. The first prior is a Jeffreys distribution between 2.5 days and five times the time span of the observations (2600), this ensures the GP model doesn't assume stellar activity could be coherent over periods longer than the observational data. The second prior is that the decay timescale is larger than half the period of recurrence ($P_{rot}/2$). This lower bound condition prevents the GP from producing stellar signals that are too close to white noise and becoming impure (Angus et al. (2018), Haywood et al. (2014)).

A.0.2 Priors for the planetary model (Sect. 3.2.2)

The TESS analysis performed by D21 is the source of the prior pdfs for the planetary periods we are investigating (P). The priors follow a Gaussian prior pdf centred at the D21s posterior value and the standard deviation is equal to the largest deviation value. Similarly, for the time of conjunction (T_c), we adopt a Gaussian prior this time on the result of K19s transit light curve analysis. This choice of priors is inspired by C19. The orbital parameters $e \cos \omega$ and $e \sin \omega$ follow a joint prior, the transformation of these two parameters derive the eccentricity e and define the eccentricity prior. Both orbital parameters use a beta distribution with shape parameters a: 0.867 and b: 3.03, known as a Kipping beta distribution (Kipping 2013). The prior PDF of the time of periapsis (ω) is uniform between $-\pi$ and π . The prior PDF

of the semi-amplitude (K) follows a uniform distribution from 0 to the largest peak-to-peak value in any of the RV observations taken by the three instruments (16.8).

A.0.3 Priors for the instrumental model (Sect. 3.2.3)

The prior PDF for the systemic velocity (v_0), is a Gaussian distribution with a mean equal to the median of the ESPRESSO data before the fibre change and a variance equal to the dataset's variance. The offset between the RV instruments ($\Delta RV_{\text{post/pre}}$, $\Delta RV_{\text{HARPS/pre}}$) are Gaussian distributed with means equal to the difference of the median values of the data sets and variances equal to the sum of their variances. The prior PDFs of the activity indicators ($C_{\text{FWHM, pre}}$, $C_{\text{FWHM, post}}$, $C_{\text{S-index, pre}}$, $C_{\text{S-index, post}}$ and $C_{\text{S-index, HARPS}}$) are also Gaussian distributed with means equal to the median value of each dataset and variances equal to the respected variances. The prior PDF of the additive jitter terms ($\sigma_{RV,\text{pre}}$, $\sigma_{RV,\text{post}}$, $\sigma_{RV,\text{HARPS}}$, $\sigma_{\text{FWHM,pre}}$, $\sigma_{\text{FWHM,post}}$, $\sigma_{\text{S-index,pre}}$, $\sigma_{\text{S-index,post}}$, and $\sigma_{\text{S-index,HARPS}}$) follow a uniform distribution from zero to five times the median value of the error for each data set respectfully. As mentioned in Sect. 3.2.3 FWHM analysis using the HARPS dataset was omitted due to the poor data quality.

Table A.1 : Prior parameters for the L98-59 model.

	Prior	Source
<i>Planetary parameters</i>		
	<i>Planet b</i>	
P [days]	$\mathcal{N}(2.2531136, 1.5e-6)$	D21
T_c [BJD - 2457000]	$\mathcal{N}(1366.1708, 3e-4)$	K19
e_*		
ω [$^\circ$]	$\mathcal{U}(-\pi, \pi)$	
$e \cos \omega$	$\mathcal{B}(0.867, 3.03)$	D21
$e \sin \omega,$	$\mathcal{B}(0.867, 3.03)$	D21
K [m s $^{-1}$]	$\mathcal{U}(0, 16.8)$	D21
	<i>Planet c</i>	
P [days]	$\mathcal{N}(3.6906777, 2.6e-6)$	D21
T_c [BJD - 2457000]	$\mathcal{N}(1367.2751, 6e-4)$	K19
e_*		
ω [$^\circ$]	$\mathcal{U}(-\pi, \pi)$	
$e \cos \omega$	$\mathcal{B}(0.867, 3.03)$	D21
$e \sin \omega,$	$\mathcal{B}(0.867, 3.03)$	D21
K [m s $^{-1}$]	$\mathcal{U}(0, 16.8)$	D21
	<i>Planet d</i>	
P [days]	$\mathcal{N}(7.4507245, 8.1e-6)$	D21
T_c [BJD - 2457000]	$\mathcal{N}(1362.7375, 8e-4)$	K19
e_*		
ω [$^\circ$]	$\mathcal{U}(-\pi, \pi)$	
$e \cos \omega$	$\mathcal{B}(0.867, 3.03)$	D21
$e \sin \omega,$	$\mathcal{B}(0.867, 3.03)$	D21
K [m s $^{-1}$]	$\mathcal{U}(0, 16.8)$	D21
<i>Stellar parameters</i>		
A_{RV}	$\mathcal{U}(0, 16.8)$	
A_{FWHM}	$\mathcal{U}(0, 0.03755)$	
$A_{S-index}$	$\mathcal{U}(0, 1.25)$	
P_{rot} [m s $^{-1}$]	$\mathcal{J}(5, 520)$	D21
λ_p [m s $^{-1}$]	$\mathcal{U}(0.05, 5)$	D21
λ_e [m s $^{-1}$]	$\mathcal{J}(2.5, 2600) + > P_{rot}/2$	D21

Table A.1 - Continued from the previous page.

	Prior	Source
<i>Instrumental parameters</i>		
v_0 [m s ⁻¹]	$\mathcal{N}(-5579.2, 35)$	
$\Delta RV_{\text{post/pre}}$	$\mathcal{N}(2.86, 4.65)$	
$\Delta RV_{\text{HARPS/pre}}$	$\mathcal{N}(-99.4, 4.9)$	
$\sigma_{RV,\text{pre}}$	$\mathcal{U}(0, 3.97059)$	
$\sigma_{RV,\text{post}}$	$\mathcal{U}(0, 3.28532)$	
$\sigma_{RV,\text{HARPS}}$	$\mathcal{U}(0, 10.5)$	
$C_{\text{FWHM, pre}}$	$\mathcal{N}(4.50518, 0.0086)$	
$C_{\text{FWHM, post}}$	$\mathcal{N}(4.5169, 0.0103)$	
$\sigma_{\text{FWHM,pre}}$,	$\mathcal{U}(0, 7.941)$	
$\sigma_{\text{FWHM,post}}$,	$\mathcal{U}(0, 6.571)$	
$C_{\text{S-index, pre}}$	$\mathcal{N}(0.633095, 0.09636)$	
$C_{\text{S-index, post}}$	$\mathcal{N}(0.685562, 0.0769)$	
$C_{\text{S-index, HARPS}}$	$\mathcal{N}(0.72, 0.14663)$	
$\sigma_{\text{S-index,pre}}$	$\mathcal{U}(0, 0.0127)$	
$\sigma_{\text{S-index,post}}$	$\mathcal{U}(0, 0.010445)$	
$\sigma_{\text{S-index,HARPS}}$	$\mathcal{U}(0, 0.7)$	

Appendix B: Posterior Samples

The posterior samples from the RV analysis in presented in Sect. 4 are detailed below. To aid the readability of this section we only provide posterior distributions for the models we graphically analysed in Sect. 4. We look at the RV-only models in Sect. B and the RV, FWHM and S-index models in Sect. B.0.1.

RV GP

Planets c and d

2D Marginalised Posterior

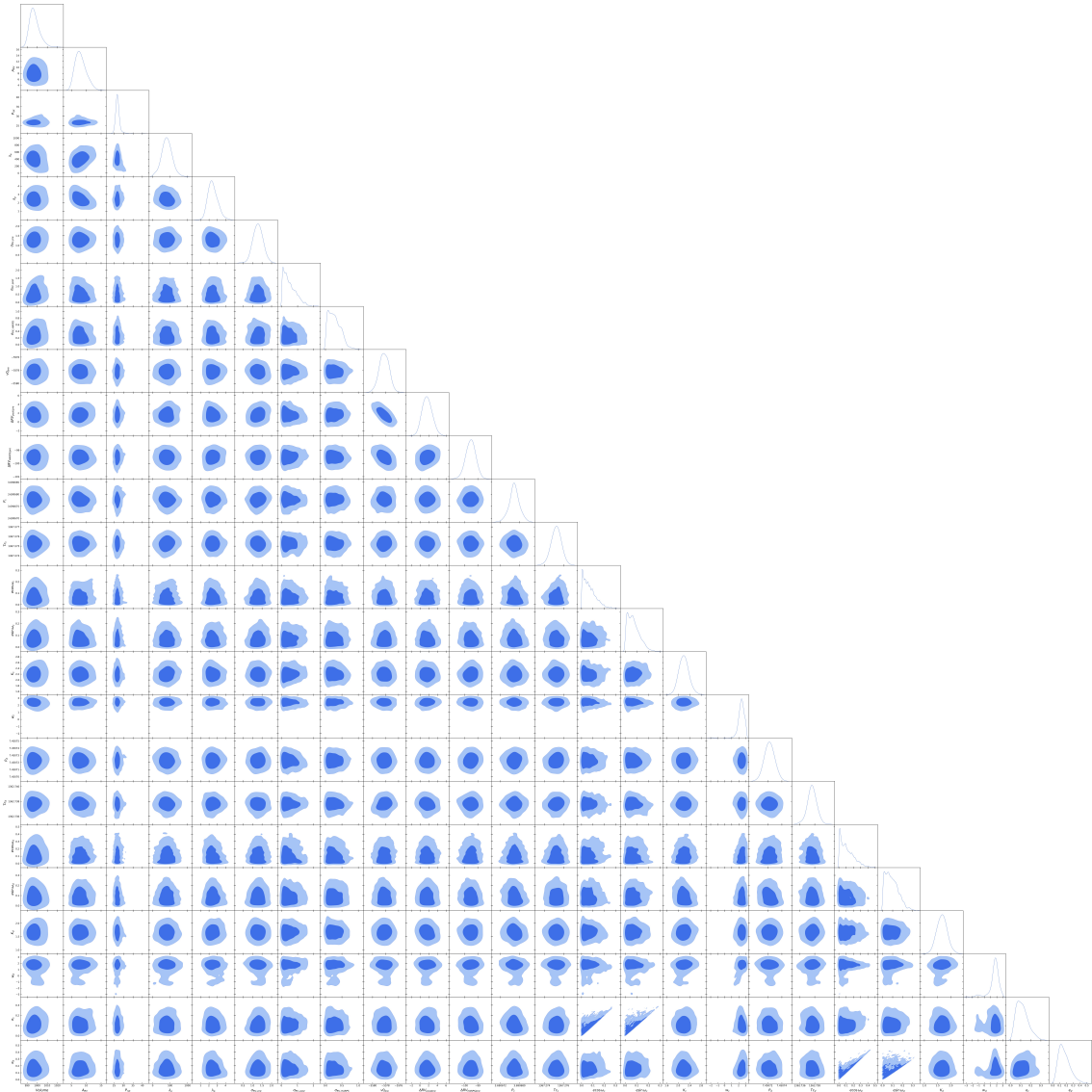


Fig. B.1 Marginalised posterior PDFs for the L98-59 system, for the two planet model using an RV-only GP.

Posterior Samples

Table B.1 : Posterior parameters for the model with three planetary signals using an RV and FWHM GP.

Posterior	
<i>Stellar parameters</i>	
A_{RV} [m s $^{-1}$]	$8.09^{+1.46}_{-2.28}$
P_{rot} [m s $^{-1}$]	$26.92^{+0.77}_{-1.17}$
λ_e [m s $^{-1}$]	$404.84^{+121.38}_{-151.91}$
λ_p [m s $^{-1}$]	$2.46^{+0.49}_{-0.68}$
<i>Instrumental parameters</i>	
$\sigma_{RV,pre}$ [m s $^{-1}$]	$1.29^{+0.27}_{-0.27}$
$\sigma_{RV,post}$ [m s $^{-1}$]	$0.52^{+0.16}_{-0.49}$
$\sigma_{RV,HARPS}$ [m s $^{-1}$]	$0.28^{+0.16}_{-0.25}$
$v0_{pre}$ [m s $^{-1}$]	$-5578.22^{+0.77}_{-0.77}$
$\Delta RV_{post/pre}$ [m s $^{-1}$]	$1.64^{+1.08}_{-1.28}$
$\Delta RV_{HARPS/pre}$ [m s $^{-1}$]	$-99.54^{+0.38}_{-0.38}$
<i>Planetary parameters</i>	
P_c [days]	$3.69^{+0.00}_{-0.00}$
Tc_c [BJD - 2457000]	$1367.28^{+0.00055}_{-0.00055}$
$e \cos \omega_c$	$0.07^{+0.02}_{-0.07}$
$e \sin \omega_c$	$0.07^{+0.02}_{-0.07}$
K_c [m s $^{-1}$]	$2.20^{+0.16}_{-0.19}$
e_c	$0.11^{+0.05}_{-0.07}$
w_c [$^{\circ}$]	$2.34^{+0.49}_{-0.32}$
P_d [days]	$7.45^{+0.00}_{-0.00}$
Tc_d [BJD - 2457000]	$1362.74^{+0.00067}_{-0.00067}$
$e \cos \omega_d$	$0.12^{+0.06}_{-0.12}$
$e \sin \omega_d$	$0.09^{+0.04}_{-0.08}$
K_d [m s $^{-1}$]	$1.66^{+0.20}_{-0.20}$
e_d	$0.17^{+0.09}_{-0.10}$
w_d [$^{\circ}$]	$1.58^{+0.77}_{-0.34}$

B.0.1 Planets b,c and d

2D Marginalised Posterior

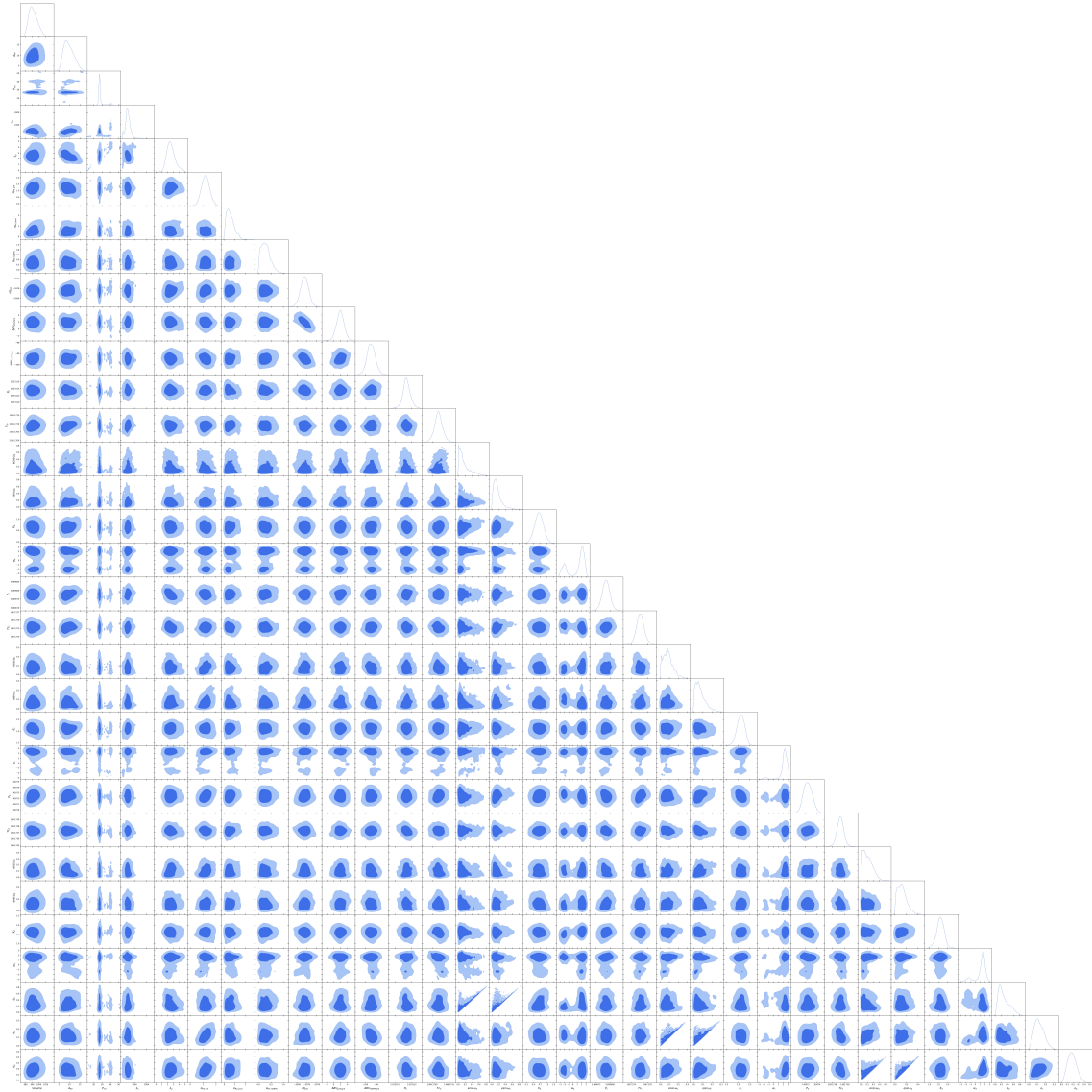


Fig. B.2 Marginalised posterior PDFs for the L98-59 system, for the three planet model using an RV-only GP.

Posterior Samples

Table B.2 : Posterior parameters for the model with three planetary signals using an RV-only GP.

Posterior	
<i>Stellar parameters</i>	
A_{RV} [m s $^{-1}$]	$9.63^{+2.40}_{-2.90}$
P_{rot} [m s $^{-1}$]	$27.85^{+0.16}_{-2.00}$
λ_e [m s $^{-1}$]	$464.69^{+177.56}_{-200.57}$
λ_p [m s $^{-1}$]	$2.58^{+0.54}_{-0.88}$
<i>Instrumental parameters</i>	
$\sigma_{RV,pre}$ [m s $^{-1}$]	$1.19^{+0.32}_{-0.32}$
$\sigma_{RV,post}$ [m s $^{-1}$]	$0.57^{+0.20}_{-0.46}$
$\sigma_{RV,HARPS}$ [m s $^{-1}$]	$0.30^{+0.19}_{-0.24}$
$v0_{pre}$ [m s $^{-1}$]	$-5578.50^{+0.86}_{-0.85}$
$\Delta RV_{post/pre}$ [m s $^{-1}$]	$1.88^{+1.13}_{-1.13}$
$\Delta RV_{HARPS/pre}$ [m s $^{-1}$]	$-99.46^{+0.38}_{-0.38}$
<i>Planetary parameters</i>	
P_b [days]	$2.25^{+0.00}_{-0.00}$
Tc_b [BJD - 2457000]	$1366.17^{+0.00025}_{-0.00025}$
$e \cos \omega_b$	$0.19^{+0.04}_{-0.19}$
$e \sin \omega_b$	$0.17^{+0.05}_{-0.16}$
K_b [m s $^{-1}$]	$0.65^{+0.20}_{-0.18}$
e_b	$0.29^{+0.09}_{-0.23}$
w_b [$^{\circ}$]	$0.79^{+2.15}_{-3.15}$
P_c [days]	$3.69^{+0.00}_{-0.00}$
Tc_c [BJD - 2457000]	$1367.28^{+0.00049}_{-0.00049}$
$e \cos \omega_c$	$0.08^{+0.03}_{-0.08}$
$e \sin \omega_c$	$0.07^{+0.03}_{-0.07}$
K_c [m s $^{-1}$]	$2.11^{+0.18}_{-0.16}$
e_c	$0.12^{+0.06}_{-0.07}$
w_c [$^{\circ}$]	$2.00^{+0.91}_{-1.12}$
P_d [days]	$7.45^{+0.00}_{-0.00}$
Tc_d [BJD - 2457000]	$1362.74^{+0.00057}_{-0.00057}$
$e \cos \omega_d$	$0.11^{+0.04}_{-0.11}$
$e \sin \omega_d$	$0.12^{+0.05}_{-0.12}$
K_d [m s $^{-1}$]	$1.60^{+0.21}_{-0.19}$
e_d	$0.18^{+0.07}_{-0.09}$
w_d [$^{\circ}$]	$1.10^{+1.14}_{-1.91}$

RV, FWHM and S-index GP

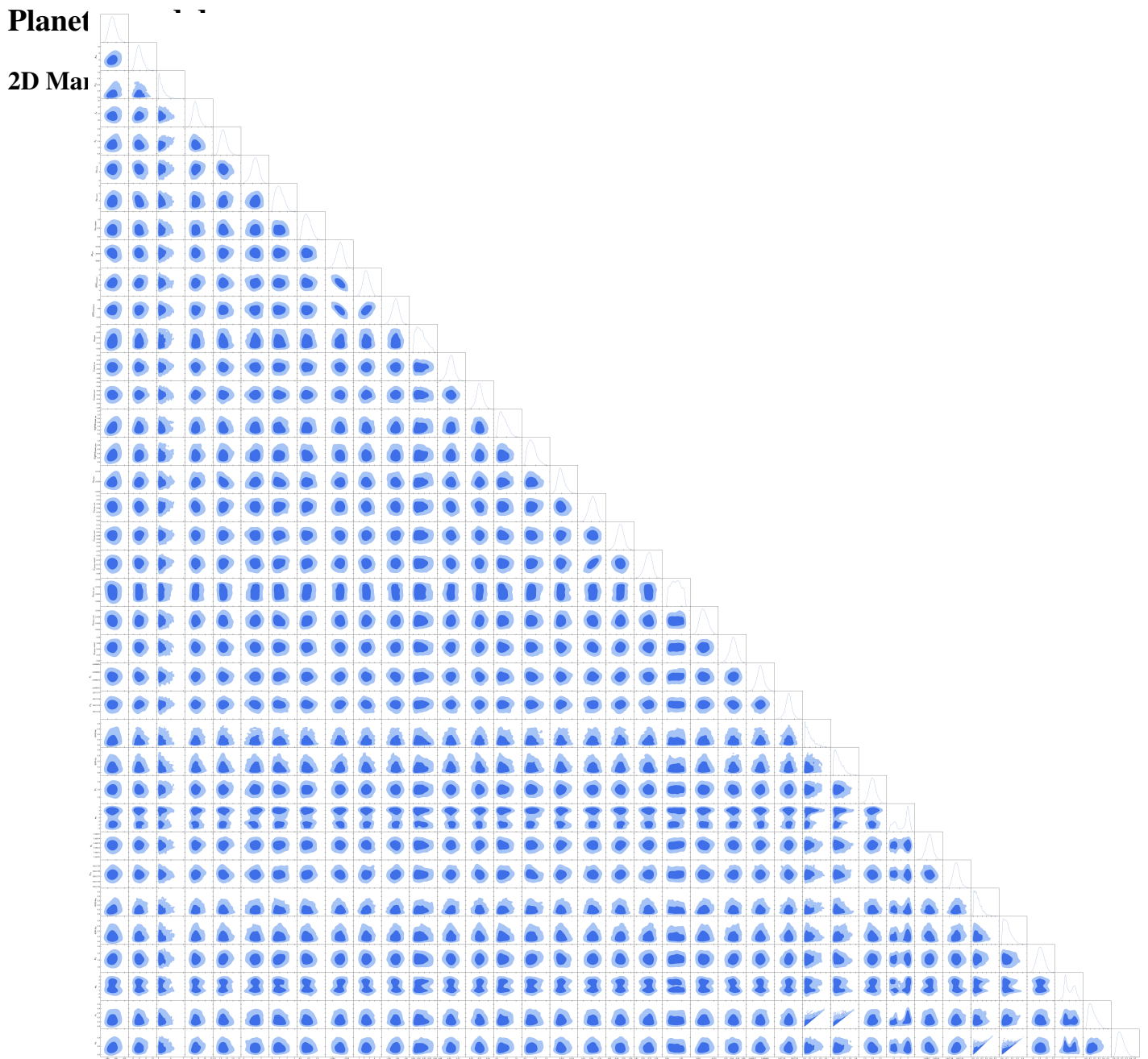


Fig. B.3 Marginalised posterior PDFs for the L98-59 system, for the two planet model using an RV, FWHM and S-index GP.

Posterior Samples

Table B.3 : Posterior parameters for the model with two planetary signals using an RV, FWHM and S-index GP.

	Posterior
<i>Stellar parameters</i>	
A_{RV} [m s $^{-1}$]	$5.96^{+0.76}_{-1.19}$
A_{FWHM} [km s $^{-1}$]	$0.014^{+0.003}_{-0.011}$
$A_{S\text{-index}}$	$0.0098^{+0.002}_{-0.005}$
P_{rot} [m s $^{-1}$]	$5.32^{+0.06}_{-0.32}$
λ_e [m s $^{-1}$]	$13.34^{+1.90}_{-3.28}$
λ_p [m s $^{-1}$]	$1.25^{+0.29}_{-0.35}$
<i>Instrumental parameters</i>	
$v_{0,pre}$ [m s $^{-1}$]	$-5578.93^{+0.50}_{-0.50}$
$\Delta RV_{post/pre}$ [m s $^{-1}$]	$2.43^{+0.67}_{-0.70}$
$\Delta RV_{HARPS/pre}$ [m s $^{-1}$]	$-99.19^{+0.40}_{-0.40}$
$\sigma_{RV,pre}$ [m s $^{-1}$]	$1.29^{+0.25}_{-0.40}$
$\sigma_{RV,post}$ [m s $^{-1}$]	$0.97^{+0.82}_{-0.57}$
$\sigma_{RV,HARPS}$ [m s $^{-1}$]	$0.41^{+0.19}_{-0.26}$
$C_{FWHM,pre}$ [km s $^{-1}$]	$4.50^{+0.008}_{-0.008}$
$C_{FWHM,post}$ [km s $^{-1}$]	$4.52^{+0.008}_{-0.008}$
$\sigma_{FWHM,pre}$ [m s $^{-1}$]	$0.34^{+0.12}_{-0.29}$
$\sigma_{FWHM,post}$ [m s $^{-1}$]	$0.33^{+0.13}_{-0.25}$
$C_{S\text{index},pre}$	$0.67^{+0.02}_{-0.02}$
$C_{S\text{index},post}$	$0.68^{+0.02}_{-0.02}$
$C_{S\text{index},HARPS}$	$0.72^{+0.02}_{-0.02}$
$\sigma_{S\text{index},pre}$	$0.0063^{+0.003}_{-0.004}$
$\sigma_{S\text{index},post}$	$0.0068^{+0.001}_{-0.005}$
$\sigma_{S\text{index},HARPS}$	$0.045^{+0.012}_{-0.029}$
<i>Planetary parameters</i>	
P_c [days]	$3.69^{+0.00}_{-0.00}$
$T c_c$ [BJD - 2457000]	$1367.28^{+0.0005}_{-0.0005}$
$e \cos \omega_c$	$0.094^{+0.025}_{-0.094}$
$e \sin \omega_c$	$0.097^{+0.026}_{-0.097}$
K_c [m s $^{-1}$]	$1.99^{+0.19}_{-0.24}$
e_c	$0.149^{+0.054}_{-0.108}$
w_c [$^\circ$]	$0.47^{+1.27}_{-2.75}$

Table B.3 - Continued from the previous page.

Posterior	
<i>Planetary parameters</i>	
P_d [days]	$7.45^{+0.00}_{-0.00}$
Tc_d [BJD - 2457000]	$1362.74^{+0.0007}_{-0.0007}$
$e \cos \omega_d$	$0.11^{+0.03}_{-0.11}$
$e \sin \omega_d$	$0.11^{+0.03}_{-0.11}$
K_d [m s^{-1}]	$1.57^{+0.27}_{-0.29}$
e_d	$0.171^{+0.084}_{-0.113}$
w_d [$^\circ$]	$0.16^{+1.21}_{-1.73}$

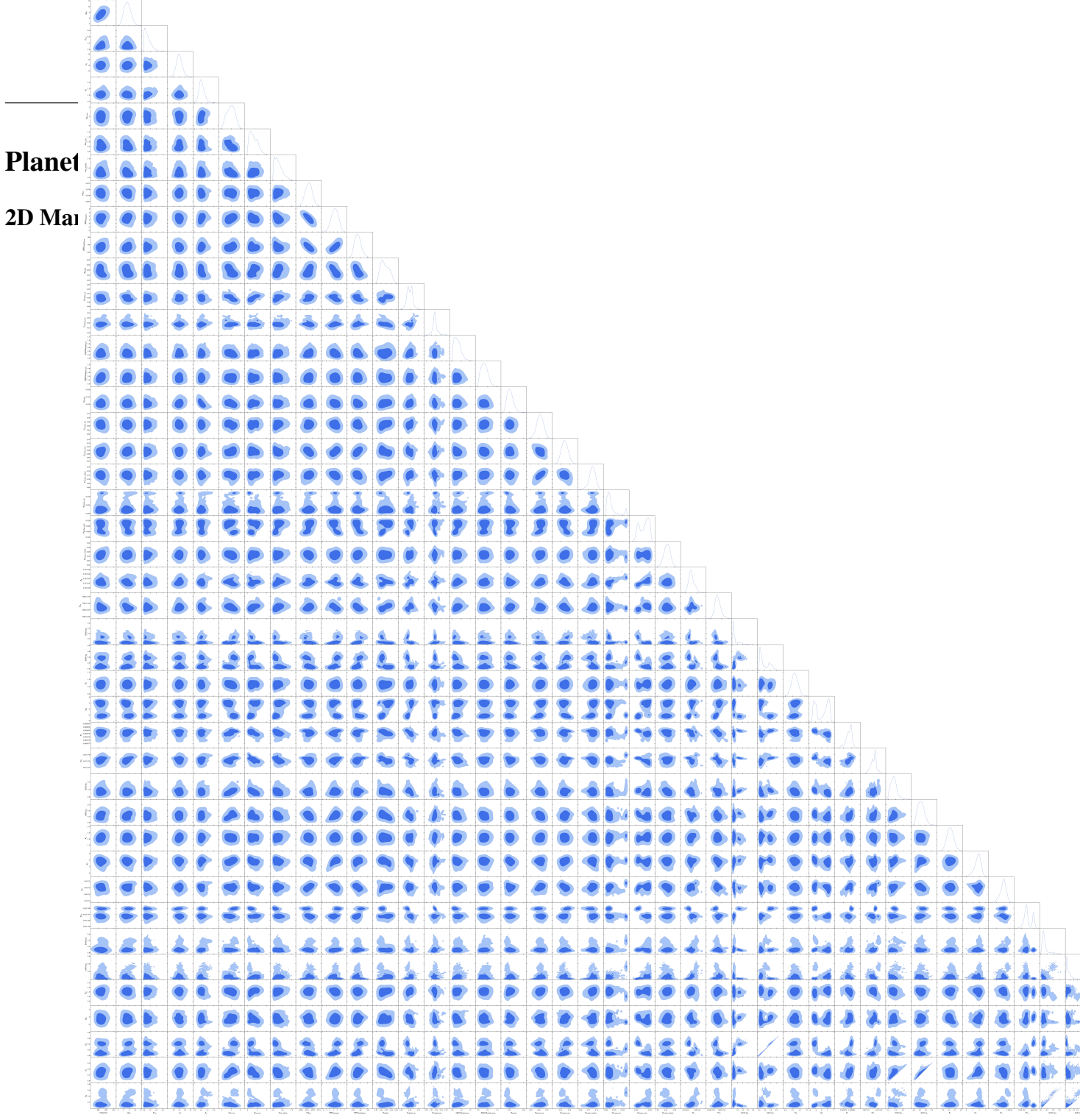


Fig. B.4 Marginalised posterior PDFs for the L98-59 system, for the three planet model using an RV, FWHM and S-index GP.

Posterior Samples

Table B.4 : Posterior parameters for the model with three planetary signals using an RV, FWHM and S-index GP.

	Posterior
<i>Stellar parameters</i>	
A_{RV} [m s ⁻¹]	$7.31^{+1.10}_{-1.32}$
A_{FWHM} [km s ⁻¹]	$0.017^{+0.007}_{-0.011}$
$A_{S\text{-index}}$	$0.0107^{+0.002}_{-0.003}$
P_{rot} [m s ⁻¹]	$5.33^{+0.09}_{-0.33}$
λ_e [m s ⁻¹]	$14.95^{+2.99}_{-2.80}$
λ_p [m s ⁻¹]	$1.06^{+0.21}_{-0.25}$
<i>Instrumental parameters</i>	
$v_{0,pre}$ [m s ⁻¹]	$-5578.62^{+0.58}_{-0.58}$
$\Delta RV_{post/pre}$ [m s ⁻¹]	$1.36^{+0.66}_{-0.95}$
$\Delta RV_{HARPS/pre}$ [m s ⁻¹]	$-99.28^{+0.45}_{-0.45}$
$\sigma_{RV,pre}$ [m s ⁻¹]	$0.96^{+0.45}_{-0.55}$
$\sigma_{RV,post}$ [m s ⁻¹]	$0.63^{+0.42}_{-0.55}$
$\sigma_{RV,HARPS}$ [m s ⁻¹]	$0.30^{+0.21}_{-0.26}$
$C_{FWHM,pre}$ [km s ⁻¹]	$4.50^{+0.007}_{-0.006}$
$C_{FWHM,post}$ [km s ⁻¹]	$4.52^{+0.006}_{-0.005}$
$\sigma_{FWHM,pre}$ [m s ⁻¹]	$0.29^{+0.11}_{-0.24}$
$\sigma_{FWHM,post}$ [m s ⁻¹]	$0.33^{+0.15}_{-0.22}$
$C_{S\text{index},pre}$	$0.67^{+0.02}_{-0.02}$
$C_{S\text{index},post}$	$0.67^{+0.02}_{-0.02}$
$C_{S\text{index},HARPS}$	$0.72^{+0.02}_{-0.02}$
$\sigma_{S\text{index},pre}$	$0.0036^{+0.003}_{-0.003}$
$\sigma_{S\text{index},post}$	$0.0078^{+0.002}_{-0.002}$
$\sigma_{S\text{index},HARPS}$	$0.0458^{+0.015}_{-0.029}$
<i>Planetary parameters</i>	
P_b [days]	$2.25^{+0.00}_{-0.00}$
$T c_b$ [BJD - 2457000]	$1366.17^{+0.0002}_{-0.0002}$
$e \cos \omega_b$	$0.06^{+0.01}_{-0.06}$
$e \sin \omega_b$	$0.19^{+0.23}_{-0.19}$
K_b [m s ⁻¹]	$0.65^{+0.22}_{-0.22}$
e_b	$0.20^{+0.26}_{-0.20}$
w_b [°]	$0.13^{+2.93}_{-3.47}$

Table B.4 - Continued from the previous page.

	Posterior
<i>Planetary parameters</i>	
P_c [days]	$3.69^{+0.00}_{-0.00}$
Tc_c [BJD - 2457000]	$1367.28^{+0.0005}_{-0.0005}$
$e \cos \omega_c$	$0.08^{+0.03}_{-0.08}$
$e \sin \omega_c$	$0.12^{+0.06}_{-0.12}$
K_c [m s^{-1}]	$2.10^{+0.27}_{-0.34}$
e_c	$0.15^{+0.06}_{-0.11}$
w_c [$^\circ$]	$1.73^{+1.16}_{-1.84}$
P_d [days]	$7.45^{+0.00}_{-0.00}$
Tc_d [BJD - 2457000]	$1362.74^{+0.0007}_{-0.0007}$
$e \cos \omega_d$	$0.13^{+0.03}_{-0.13}$
$e \sin \omega_d$	$0.08^{+0.10}_{-0.08}$
K_d [m s^{-1}]	$1.52^{+0.34}_{-0.30}$
e_d	$0.17^{+0.14}_{-0.12}$
w_d [$^\circ$]	$0.16^{+1.38}_{-1.73}$

Appendix C: RV and FWHM GP

This model was selected for the folded-phase analysis in Sect. 4.4. This models the RV and FWHM using a GP and is modelling a three-planet system as we are trying to resolve L98-59b.

2D Marginalised posterior PDFs

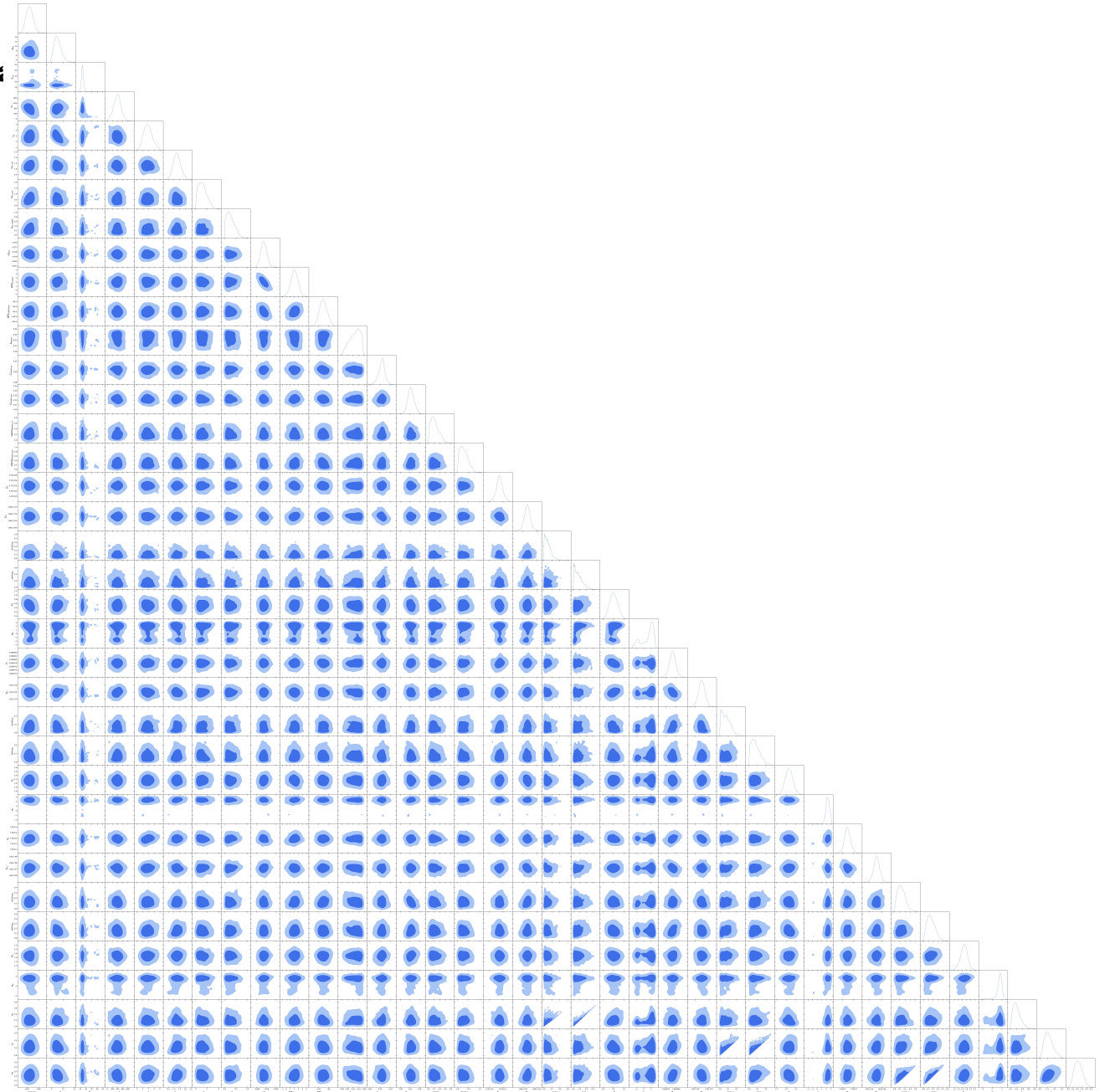


Fig. C.1 Marginalised posterior PDFs for the L98-59 system, for the three planet model using an RV and FWHM GP.

GP Fit and Periodogram

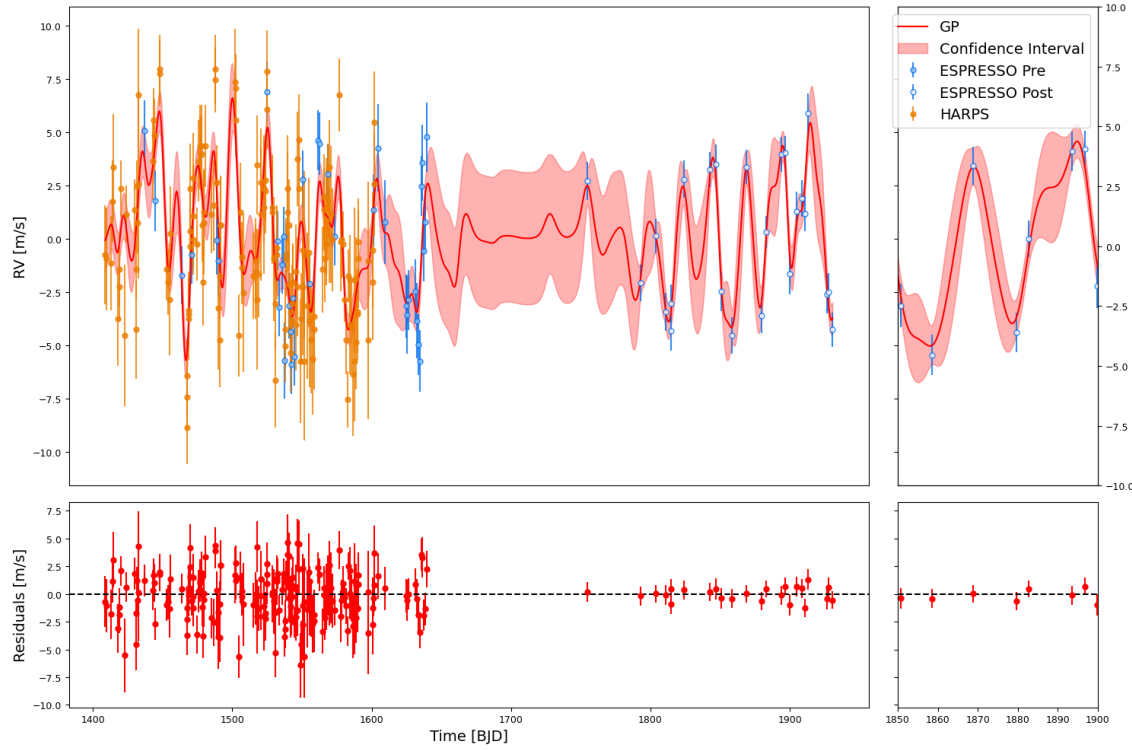


Fig. C.2 GP model fit, trained on RV and FWHM, applied to RV data for a three-planet system, plotted with observed RV data and model predictions. The top panel displays the GP model fit with a 1σ confidence interval alongside the observed RV data points for all instruments. The bottom panel shows the residuals of the fit.

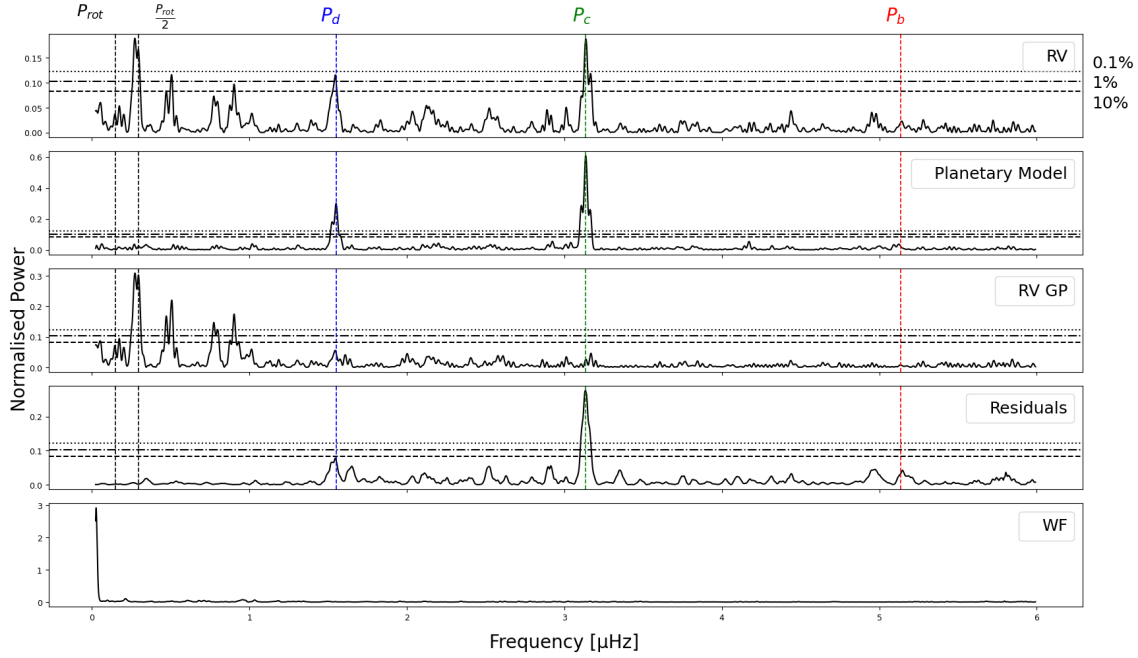


Fig. C.3 Periodogram analysis of a three-planet system, detailing RV data, planetary model outputs, GP model fit (RV) and residuals. As well as marks indicating the rotation periods (P_{rot} , $P_{rot}/2$) and planetary periods (P_b , P_c , P_d).

Posterior Samples

Table C.1 : Posterior parameters for the model with three planetary signals using an RV and FWHM GP.

	Posterior
<i>Stellar parameters</i>	
A_{RV} [m s $^{-1}$]	$7.71^{+1.25}_{-1.93}$
A_{FWHM} [km s $^{-1}$]	$0.0227^{+0.011}_{-0.019}$
P_{rot} [m s $^{-1}$]	$27.38^{+0.41}_{-1.58}$
λ_e [m s $^{-1}$]	$382.80^{+91.01}_{-139.75}$
λ_p [m s $^{-1}$]	$2.92^{+0.66}_{-0.87}$
<i>Instrumental parameters</i>	
$v0_{pre}$ [m s $^{-1}$]	$-5578.51^{+0.70}_{-0.70}$
$\Delta RV_{post/pre}$ [m s $^{-1}$]	$2.00^{+0.92}_{-1.50}$
$\Delta RV_{HARPS/pre}$ [m s $^{-1}$]	$-99.50^{+0.39}_{-0.39}$
$\sigma_{RV,pre}$ [m s $^{-1}$]	$1.27^{+0.31}_{-0.35}$
$\sigma_{RV,post}$ [m s $^{-1}$]	$0.60^{+0.22}_{-0.49}$
$\sigma_{RV,HARPS}$ [m s $^{-1}$]	$0.27^{+0.10}_{-0.26}$
$C_{FWHM,pre}$ [km s $^{-1}$]	$4.50^{+0.006}_{-0.005}$
$C_{FWHM,post}$ [km s $^{-1}$]	$4.52^{+0.007}_{-0.007}$
$\sigma_{FWHM,pre}$ [m s $^{-1}$]	$0.23^{+0.08}_{-0.19}$
$\sigma_{FWHM,post}$ [m s $^{-1}$]	$0.28^{+0.09}_{-0.18}$
<i>Planetary parameters</i>	
P_b [days]	$2.25^{+0.00}_{-0.00}$
Tc_b [BJD - 2457000]	$1366.17^{+0.0002}_{-0.0002}$
$e \cos \omega_b$	$0.11^{+0.03}_{-0.10}$
$e \sin \omega_b$	$0.17^{+0.11}_{-0.16}$
K_b [m s $^{-1}$]	$0.51^{+0.20}_{-0.21}$
e_b	$0.22^{+0.13}_{-0.17}$
w_b [$^{\circ}$]	$1.00^{+2.06}_{-2.96}$
P_c [days]	$3.69^{+0.00}_{-0.00}$
Tc_c [BJD - 2457000]	$1367.28^{+0.0005}_{-0.0005}$
$e \cos \omega_c$	$0.08^{+0.03}_{-0.08}$
$e \sin \omega_c$	$0.08^{+0.06}_{-0.08}$
K_c [m s $^{-1}$]	$2.14^{+0.20}_{-0.20}$
e_c	$0.12^{+0.06}_{-0.07}$
w_c [$^{\circ}$]	$2.24^{+0.65}_{-0.33}$

Table C.1 - Continued from the previous page.

	Posterior
<i>Planetary parameters</i>	
P_d [days]	$7.45^{+0.00}_{-0.00}$
Tc_d [BJD - 2457000]	$1362.74^{+0.0007}_{-0.0007}$
$e \cos \omega_d$	$0.13^{+0.06}_{-0.13}$
$e \sin \omega_d$	$0.16^{+0.09}_{-0.11}$
K_d [m s^{-1}]	$1.67^{+0.19}_{-0.16}$
e_d	$0.22^{+0.09}_{-0.11}$
w_d [$^\circ$]	$1.32^{+0.87}_{-0.21}$